Investigating Biomedical Applications with Terahertz Pulsed Imaging in Reflection Geometry

SY, Ming Yiu

A Thesis Submitted in Partial Fulfillment of the
Requirements for the Degree of
Master of Philosophy
in
Electronic Engineering

The Chinese University of Hong Kong

August 2011

Abstract

The Terahertz (THz) band is defined as the band of frequenciesbetween0.1THz and 10THz. It lies between the microwave and infrared regions of the electromagnetic spectrum. This radiation has very low photon energy (4.1meV) and thus it does not pose any ionization hazard for biological tissues. It is strongly attenuated by water and very sensitive to water content. The characteristics of non-ionizing and high sensitivity of water make it an ideal probe for applications in many fields such as astronomy, telecommunications, national security, and biomedicine.

Unique absorption spectra due to intermolecular vibrations in this region have been found in different biological objects. These distinctive advantages over other techniques like x-ray and ultrasound make terahertz imaging very attractive for medical applications so as to provide complimentary information to existing imaging techniques.

Breast cancer and skin cancer with terahertz detection are the most outstanding examples to show the potential of Terahertz Pulsed Imaging (TPI). In fact terahertz imaging and spectroscopy techniques have only a history of about two decades due to a previous lack of terahertz sources. In the future it may become a key medical imaging technique around the world. Therefore the objective of this thesis is to conduct several pilot studies to investigate the potential and possibility of TPI being applied in medical field.

If terahertz imaging is to be used in the future for medical purposes, it is likely to be more feasible if conducted in reflection geometry and with a hand-held probe. Therefore we would prefer sensing in reflection mode to transmission mode and our machine was switched from a flat-bed system to hand-held probe system. Both *in vivo* and *ex vivo* medical experiments using TPI have been shown in this thesis.

Regarding *ex vivo* experiments, we focus on distinguishing between the normal and diseased organ and liver cirrhotic tissues is the main study target of this thesis. Liver cirrhosis is a complication of many liver diseases that lead to abnormal structural and functional degradation of the liver. To better manage individuals with progressive cirrhosis, especially those who would benefit from early intervention, a reproducible and reliable non-invasive method is needed to evaluate disease progression, to monitor responses to drug treatment, and to benefit epidemiologic research and TPI would be a good choice due to its own characteristics.

On the other hand, for *in vivo* experiments we focused on the skin studies. Skin diseases such as eczema and psoriasis cause inflamed, dry and flaky skin and one of the main symptoms of those skin diseases is the rapid change of stratum corneum thickness which is the outermost layer of human skin. As a result it would be beneficial if the severity of the condition could be quantitatively measured and monitored and thus healing methods, for example UV light and topical steroids, could be tested for effectiveness in reducing symptoms.

For further study into the impact of noise on the calculation of optical parameters, simulation work was performed and a method was developed to quantitatively assess the accuracy from the dynamic range of the sample signal.

摘要

太赫茲(THz)波是一種介於遠紅外和微波之間的電磁波譜,其頻率範圍爲 0.1—10THz。THz 輻射光子能量極低（1THz 約 4.1meV）,因而不會對人或生物有機體造成電離傷害。THz 波極易被水等極性液體吸收,因此太赫茲是理想探測工具於各種研究領域,例如：天文學、遠程通訊、國防以及生物醫學。

由於不同生物的分子具有獨特的振動特性,各類生物對 THz 波段呈現不同的吸收光譜,基於此,太赫茲成像技術相對其他技術如 X 射線和超聲波,能夠爲現有醫療成像技術提供輔助資訊,在醫學成像領域具有較大的應用潛力。

乳腺癌和皮膚癌的太赫茲檢測是太赫茲脉衝成像技術（TPI）在醫學成像領域非常成功的應用範例。過去由於太赫茲輻射源的缺乏,太赫茲成像和光譜技術只有約二十年歷史,但在不久的將來,太赫茲脉衝技術將成爲醫療成像領域的一項關鍵技術。基於此,本文將對太赫茲脉衝技術在醫療領域的潛在應用展開一些前瞻性研究。

太赫茲脉衝成像技術從成像原理上可分爲反射式成像和透射式成像,從探測系統設計上可以分爲便攜式探頭設計和固定平面式掃描系統。在醫療成像領域,反射式成像及便攜式探頭設計更具實用性。因此,本文將主要對基於反射式成像和便攜式探頭的太赫茲成像技術進行研究。爲了能夠以一個全面的角度探討太赫茲脉衝成像技術,本文將分別從生物體內及生物體外的 TPI 醫學實驗展開該技術的前沿研究。

對於生物體外實驗,本文以肝硬化組織爲例,旨在用太赫茲成像區分正常和病變器官。肝硬化是基於各種肝臟疾病而形成的一種病症,它會令病者的肝臟出現結構性以及功能性的退化。對於早期的肝硬化病人,爲了能夠更好控制其病情以及更有效監測病者對藥物治療的反應,一種可再用的、可靠的、非侵入式式肝臟監察技術是必需的,TPI基於其自身特點是一個不錯的選擇。

對於生物體內實驗,本文以皮膚爲研究對象,旨在評估一些典型的皮膚疾病如濕疹和牛皮癬的病情程度。這些皮膚疾病通常會引起皮膚發炎,乾燥以及剝落,因此角質層(人體皮膚的最外層)厚度的迅速變化是一個這類皮膚疾病的主要症狀。因此,基於變化的角質層厚度,病者的病情程度可用TPI技術進行定量測量和監控,這將有助於判斷病情進度,從而對病者施以正確的治療方法,例如紫外線和外用類固醇等療法。

最後，為了進一步研究噪聲對光學參數的影響，一項量性模擬實驗被進行用以評估樣品信號的準確動態範圍。

Acknowledgments

First and foremost, I would like to take this opportunity to express the immense gratitude to my supervisor, Professor Emma Pickwell-MacPherson, for her invaluable guidance and support during the year of my Mphil studies. I am also grateful for her patience and time spent on my study and deeply appreciates the opportunity to work under her supervision as she really broadened my horizons and gave me a lot of opportunities.

Grateful thankfulness is acknowledged to my supervisor Professor Yuan-ting Zhang for his guidance and support throughout this study and especially for his tolerance to my lots of careless mistakes and the chance for exploring the world of biomedical engineering.

I am very grateful to Professor Yi-Xiang Wang at the Department of Diagnostic Radiology and Organ Imaging. He has offered me a lot of invaluable help with my experiments and paper work.

I would like to thank all the colleagues in JCBME for their help, especially Dr Shengyang Huang, Dr Edward Parrott, Dr Yiwen Sun, Dr. Yang Chen and Ms. Kanis Kan

Finally I would like to thank my family and friends for their support.

Table of Contents

List of figures

List of tables

List of abbreviations

AC   Absorption Coefficient

CW   Continuous Wave

DGF   Double Gaussian Filter

DR   Dynamic Range

EMS   Electromagnetic Spectrum

EC   Extinction Coefficient

FDHM   Full Duration at Half Maximum

FWHM   Full Width at Half Maximum

HCC   Hepatocellular Carcinoma

KHS   Krebs-Henseleit Solution

MAD   Maximum Absolute Differences

MPD   Maximum Percentage Difference

RI   Refractive Index

RMS   Root Mean Square

SC   Stratum Corneum

SNR   Signal to Noise Ratio

STD   Standard Deviation

TEM   Transverse Electromagnetic

THz-TDS   Terahertz Time Domain Spectroscopy

TPI   Terahertz Pulsed Imaging

TPS   Terahertz Pulsed Spectroscopy

List of publications and awards

Journal articles

1. Parrott E.P.J, **Sy M.Y**, Blu T, Wallace V.P, Pickwell-Macpherson E. Terahertz pulsed imaging in vivo: measurements and processing methods. *Journal of Biomedical Optics.* 2011 (under review)

2. Sun Y, **SyMY**, Wang YX, Ahujab AT, Zhang YT, Pickwell-MacPherson E. A promising diagnostic method – terahertz pulsed imaging and spectroscopy. *World Journal of Radiology.* 2011; **3**(3).

3. **SyMY**, Huang SY, Wang Y-XJ, Yu J, Ahuja AT, Zhang Y-T, et al. Terahertz spectroscopy of liver cirrhosis: Investigating the origin of contrast. *Physics in Medicine and Biology.* 2010; **55**(24): 7587.

Conference articles

2. **SyMY**, Zhang YT, Pickwell-Macphersone E. A Study of Terahertz Pulsed Imaging of Human Skin under Different Temperature. T*he 7th International School and Symposium on Medical Devices and Biosensors, in conjunction with The 5th International School and Symposium on Biomedical and Health Engineering,*; Hong Kong, December 2010.

3. **Sy MY**, Huang SY, Wang Y.X, Ahuja AT, Zhang YT, Pickwell-Macpherson E, Investigating the role of water content on the terahertz properties of rat liver cirrhosis. *Infrared Millimeter and Terahertz Waves (IRMMW-THz), 2010 35th International Conference on*; 2010 5-10 Sept. 2010.

4. **Sy MY**, Zhang YT, Pickwell-MacPherson E, A study of tpi of human skin under different temperature and humidity. *Infrared Millimeter and Terahertz Waves (IRMMW-THz), 2010 35th International Conference on*; 2010 5-10 Sept. 2010.

5. **Sy MY**,Chen Y, Zhang YT, Pickwell-Macphersone E. A study of terahertz pulsed imaging of human skin. T*he 6th International School and Symposium on Medical*

Devices and Biosensors, in conjunction with The 4th International School and Symposium on Biomedical and Health Engineering,; Shenzhen, December 2009.

6. Gu WB, Poon CCY, Leung HK, **Sy MY**, Wong MYM, Zhang YT, A novel method for the contactless and continuous measurement of arterial blood pressure on a sleeping bed. *Engineering in Medicine and Biology Society, 2009. EMBC 2009. Annual International Conference of the IEEE*; 2009 3-6 Sept. 2009. (**)

7. Gu WB, Poon CCY, **Sy MY**, Leung HK, Liang YP, Zhang YT, A h-shirt-based body sensor network for cuffless calibration and estimation of arterial blood pressure. *Wearable and Implantable Body Sensor Networks, 2009. BSN 2009. Sixth International Workshop on*; 2009 3-5 June 2009. (**)

(**):The work for them is not about terahertz but developing a new device for monitoring cardiovascular diseases. The hardware development is my main contribution to those projects. During those projects, under the guidance of Professor Y.T Zhang I have gain a lot of knowledge about cardiovascular disease (i.e the pathology, symptoms and causes) which really helps me to know more about the road of research and inspires me having several ideas for using terahertz on cardiovascular diseases diagnosis.

Awards

1. Global Moot Corp Competition 2010: Outstanding Product Award (Austin, USA)

   (This is an international competition about technology transferring from school to market. In which four MBA students in CUHK and me had to think about how to practically and successfully transfer our own cardiovascular device to the market.)

2. The Chinese University of Hong Kong VCC of Student Entrepreneurship 2010: Champion Team

   (This is a CUHK internal competition about creating some creative and outstanding products also we have to deal with the commercialization and mass production process practically.)

3. The Chinese University of Hong Kong VCC of Student Innovation 2009 :2nd Runner-up

   (This is a CUHK internal competition only for engineering students. In which our team developed a novel non-contact technique for measuring the photoplethysmograph (PPG) on patient during sleeping.)

Chapter 1 Introduction

Interest in Terahertz Pulsed Imaging (TPI) is rapidly expanding and we can see the number of journal papers related to terahertz has increased sharply recently (shown in Figure 1.1), especially in biological and medical applications, yet they are still in their infancies compared with other popular imaging techniques such as "MRI", "X-ray" and "Ultrasound". In this thesis, we aim to further study terahertz imaging in biological tissues both *in vivo* and *ex vivo* in order to demonstrate its potential to become a new diagnosis tool in next generation using our reflection terahertz system with a hand-held probe. Also, compared with conventional modalities, THz has its own advantages (shown in Table 1.1). This thesis presents a number of novel analysis techniques and some pilot medical applications. All of them are important steps along the road to verify Terahertz Pulsed Imaging as a reliable technique used in clinical applications and in future.
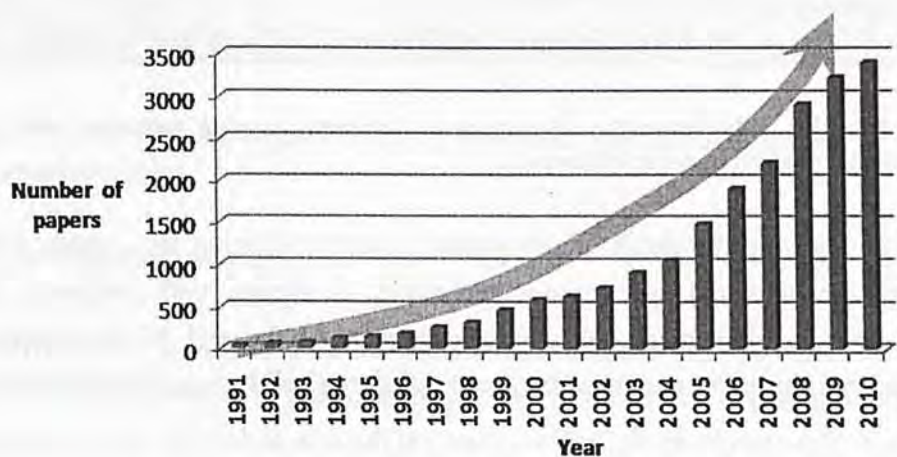
Figure 1.1: Number of journal papers topic related with Terahertz (source from ISI)

Terahertz V.S	Advantages (of terahertz)
X-Ray:	• Non-ionizing (not harmful) • Able to probe small density change in soft tissues
MRI:	• Lower power • Better resolution • More sensitivity to many epithelial tumors • Less expensive
OCT	• Deeper penetration • Less scattering effects • More spectral information
Ultrasound	• Spectral fingerprinting • Automatic tissue classification allows for diagnostic imaging

Table 1.1: The table shown the advantages of Terahertz imaging compared with several conventional medical imaging techniques.

Before showing the detail of our works, a brief review on the current status of terahertz imaging and spectroscopy techniques is shown, with emphasis on the applications in biomedical fields in this chapter. At the end of this chapter, the motivations, objectives and the structure of this thesis will be mapped out in detail.

1.1 Terahertz radiation

Terahertz radiation ($1THz=10^{12}Hz$) is a sort of electromagnetic wave generally located between infrared and microwave of the electromagnetic spectrum. The terahertz regime is typically defined as ranging from 0.1 to 10 THz in frequency, or 3.33 $cm^{-1}$to 33.3 cm^{-1} in wave numbers ($\lambda = f/c$), and photon energies of 2.0 $\times 10^{-22}$to 1.3$\times 10^{-22}$J [1].

We are familiar with microwave and infrared radiations, which can be generated and detected by the electronic and photonic mechanisms respectively. Terahertz radiation is in the gap between them, as illustrated in Figure 1.2. It was previously known as the 'THz gap' because it was difficult to generate and detect its radiation by simple photonic or electronic devices and mechanisms.
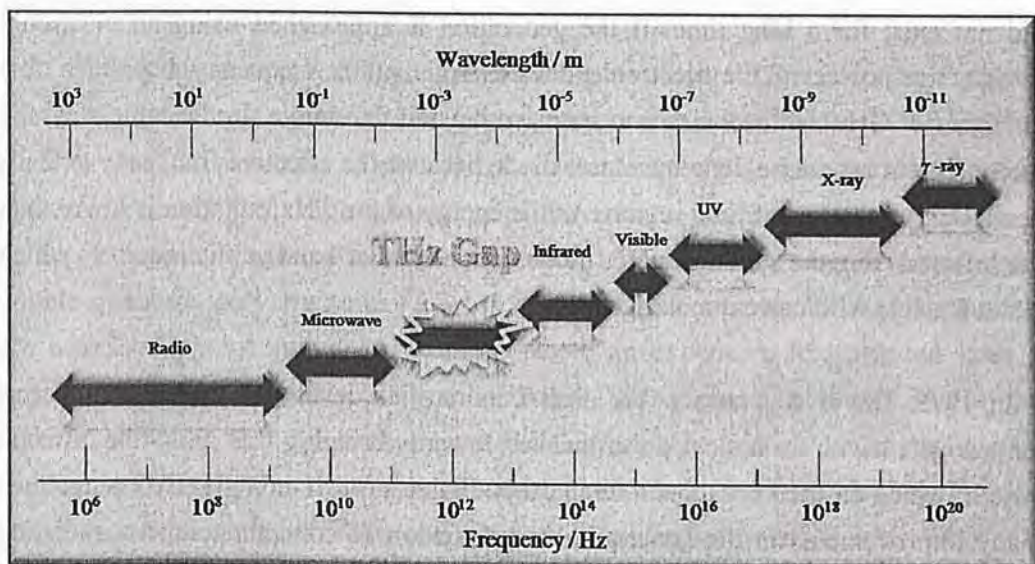
Figure 1.2: The Terahertz region of the electromagnetic spectrum lies between the infrared and microwave region.

1.1.1 Terahertz sources

THz radiation is abundant in the natural environment. For example, the human body is constantly emitting radiation in the THz range. Every object around us with temperature over 10 Kelvin emits THz wave as part of the 'black-body radiation'. Although it is very easy to find THz radiation naturally, it is not easy to employ them in scientific and technological applications as the radiation is generally 'incoherent' and very low in power which is the main obstacle for scientists to speed up the development of Terahertz.

Experiments with Terahertz radiation can date back to measurements of black body radiation using a bolometer in the 1890s [2, 3]. However, for a long time, this region

remained unexplored due to a previous lack of good sources and detectors.

The technology to generate and detect 'coherent' THz radiation in an efficient way did not exist for a long time. If the generation is approached using an electronic device, the power of the electronic devices rolls off at frequency beyond a few hundreds of GHz and becomes unresponsive beyond that range. In the same way, the measurement cannot be done by a laser diode because the effective frequency extends down only to the far infrared region. As the energy of the THz radiation is lower than the Infrared (IR), the semiconductor diode with a smaller band gap is required, which is not feasible with current materials.

In 1975, David Auston at AT&TBell Laboratories developed a photoconductive emitter gated with an optical pulse that led towards bridging this gap - the 'Auston switch' which emitted broadband terahertz radiation up to 1 mW[4]. Ever since then many improvements in the generation and detection of coherent terahertz radiation enabled terahertz time domain spectroscopy (TDS) and imaging techniques to be pioneered for applications in various fields such as astronomy[5], security screening[6], genetic engineering[7], pharmaceutical quality control[8] and medical imaging[9]. Particularly, applications in medical area are believed to be very promising but challenging.

1.1.2 Terahertz systems

Over the past two decades, technologies for generating and detecting terahertz radiation have changed considerably. Because of these advances, various terahertz systems have been set up by many groups all over the world and several commercialized systems are available now[6, 10-13]. According to the radiation source used, THz systems can be divided into two general classes: continuous wave (CW) and pulsed system.

A typical CW system can produce a single fixed frequency or several discrete frequency outputs. Some of them can be tunable. Generation for CW terahertz radiation can be achieved by approaches such as photomixing [14], free-electron lasers [15] and quantum cascade lasers [16]. Since the source spectrum of this kind of

system is narrow and sometimes only the intensity information is of interest, the data structures and post-processing are relatively simple. It is possible now to drive a whole CW system by cheap laser diodes and thus it can be made compact and inexpensive and therefore cost effective. But due to the limited information that CW systems can afford, they are sometimes confined to those applications where only features at some specific frequencies are of interest.

In pulsed systems, broadband spectrum up to several THz can be radiated. Currently, there are a number of ways to generate and detect pulsed THz radiation, such as ultrafast switching of photoconductive antennas [17], rectification of optical pulses in crystals [18], rapid screening of the surface field via photo excitation of dense electron hole plasma in semiconductors [19] and carrier tunneling in coupled double quantum well structures [20]. Among them, the most established approaches are based on photoconductive antennas, where an expensive femtosecond laser is required. Coherent detection in these techniques can record THz waves in the time domain, including both the intensity and phase information, which can be further used to obtain more details of the target, like spectral and depth information [21]. This key advantage leads coherent THz imaging and spectroscopy to a wider range of applications.

More information and detailed comparisons of these two types of systems can be found in reference [22]. Our experimental system is a commercialized imaging platform in reflection geometry. In the remaining chapters of this thesis, our discussion will be based on a pulsed type unless otherwise specified.

1.1.3 Reflection and Transmission geometries

Generally there are two geometries for all existing terahertz measurement systems; either reflection or transmission.

In the transmission mode, the emitted THz radiation is collimated to the sample and the transmitted part is detected on the opposite side. Since the THz waves have to travel through the whole sample, a common problem for a conventional transmission system is that it is very difficult to detect signals from samples that strongly absorb

terahertz radiation such as fresh tissues [23] and samples with a large thickness. In this case, very thin slices should be prepared. In order to extract the absorption coefficient, an accurate and even thickness of the object is of vital importance. However, when dealing with samples like excised biological tissues, as they are usually soft and in irregular shapes thus easy to suffer from deformation under pressure and movement, direct measurements of their thicknesses can be very difficult. Figure 1.3 shows a transmission terahertz pulsed measuring system developed by our group.
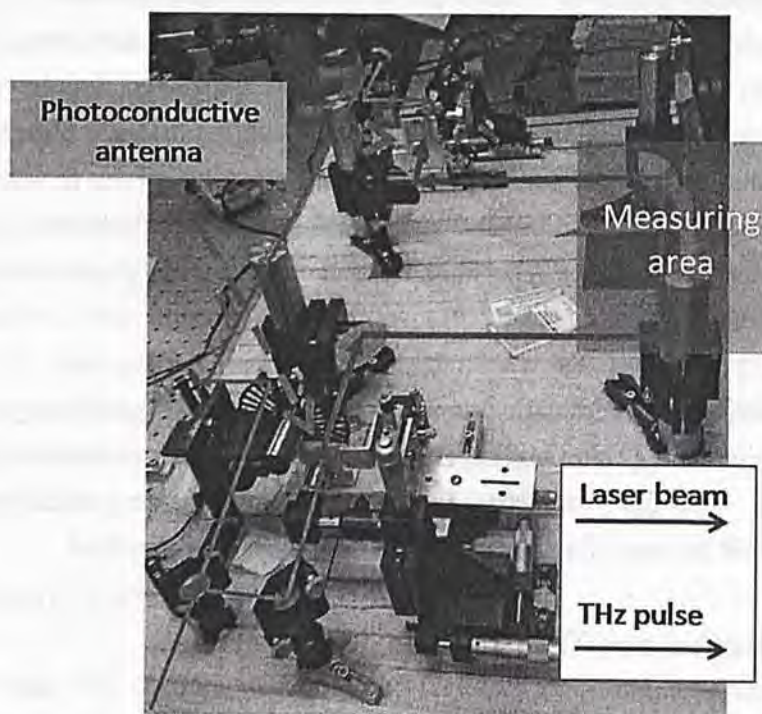
Figure 1.3: A transmission Terahertz Pulsed Imaging (TPI) system developed by our group. Red solid arrows represent the routes of the laser beam and Blue solid arrows represent the routes of Terahertz radiation. Green dotted arrows indicate both the photoconductive emitter and detector antennas. Purple shadow box represents the measuring area. [24]

Although the majority of the terahertz spectroscopy data were obtained in transmission mode in previous years (Table 1.2), in order to solve the limitation of the thickness of sample that terahertz systems in transmission mode posses, reflection geometry was recently developed, especially for applications in biological tissues. Since the detection in this geometry is from the same side as the incident THz waves,

it allows *in vivo* and *ex vivo* measurements without concern for the absorption or thickness measurement of soft samples. In addition, it can be further used to reveal the inner structure of low absorbing samples. This is possible because if the refractive index of the target layer is known, the temporal delay information between the different reflected pulses off the surface and bottom can be used to calculate the thickness of the layer. The details of our reflection Terahertz Pulsed Imaging (TPI) system will be discussed in chapter 2.

Paper	Transmission Geometry	Refection Geometry	Sample description
Arnone et al 1999 [25]	✓		Muscle, fat and kidney
Han *et al* 2000 [26]	✓		Pork muscle tissue
Loffler *et al* 2001[27]	✓		formalin-fixed, alcohol-dehydrated and paraffin-mounted samples from thin-cut canary's head
Knobloch *et al*2002[28]	✓		The larynx of a pig and a human liver with metastasis
Ferguson *et al*2002 [29]	✓		A butterfly sample and a dried chicken tissues with bone
Woodward *et al* 2003[30]		✓	Basal cell carcinoma samples
Berry *et al* 2003[31]	✓	✓	Nine types of tissues and water
Fitzgerald *et al*2003[32]	✓		Skin, adipose tissue, striated muscle, vein and nerve
Pickwell *et al*2004[33]		✓	Human skin located on palm, dorsal forearm and volar forearm
Wallace *et al* 2006[34]	✓		Excised normal skin and Basal cell carcinoma
He *et al* 2006[35]	✓		Meat and skin samples from pork and rat
Nakajima*et al*2007 [36]	✓		Paraffin-Embedded Liver tissues

Pickwell *et al*2007 [37]		✓	Bovines labs with artificial caries
Png *et al* 2008[38]	✓		Fresh and frozen rat tissues
Hoshina et al 2009 [39]	✓		Slices of frozen porcine tissue

Table 1.2: The table is a summary for previous studies using terahertz in biological aspect. And it shows whether they used the transmission or reflection system for tissue characterization.

1.2 Terahertz biomedical applications

More and more researchers and scholars are interested in Terahertz Pulsed Imaging (TPI) especially in biomedical applications and there is an increasing number of Terahertz spectra are being published. In the following section three main biological application aspects are shown.

1.2.1 Biomolecules

It has been found that the energy of rotational and vibrational transitions of molecules lies in the THz region. Terahertz spectroscopy explores low frequency motions in molecular systems. These motions are either flexing of the individual molecules themselves or intermolecular interactions, either via strong hydrogen bonds or weaker van der Waals bonding between nearest neighbors. Three main vibrational modes of water (1. Symmetric stretch (V1), 2. Bend (V2) and 3. Asymmetric stretch (V3)) are illustrated in Figure 1.4. These unique spectral features could be used to distinguish between different materials, recognize a certain material, and even determine the composition of unknown objects. A study conducted by Fischer *et al* showed that ribonucleic acid (RNA) containing different DNA bases can be distinguished by terahertz spectroscopic techniques [40]. They used terahertz time-domain spectroscopy to measure the dielectric function of two artificial RNA single strands, composed of polyadenylic acid (poly-A) and polycytidylic acid (poly-C). They found a significant difference in the absorption between the two types

of RNA strands. Polymorphism is a common issue in the pharmaceutical industry and determining the polymorphic form of a drug is very important as it can significantly affect the bioavailability and physiochemical response [13].
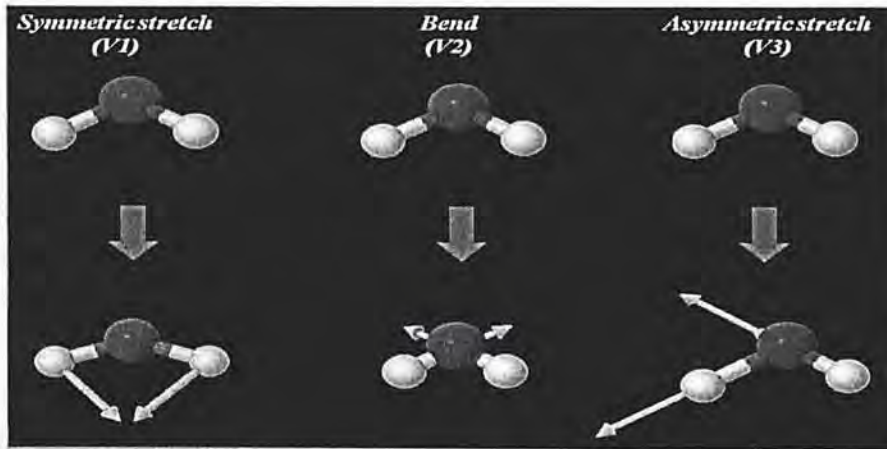
Figure 1.4: Three main vibration modes in water. 1. Symmetric stretch (V1), 2. Bend (V2) 3.Asymmetric stretch (V3) (from left to right).

1.2.2 THz biomedical imaging

Several unique features make terahertz very suitable for medical applications. For example, it has very low photon energy (1 THz = 4.1 meV), one million times weaker than X-rays, and thus will not cause harmful ionization in biological tissues; this makes it very attractive for medical applications.

One potential application of THz imaging is the diagnosis of skin cancer. The first *ex vivo* measurements on skin cancer demonstrating the ability of TPI to differentiate basal cell carcinoma (BCC) from normal skin was produced by Woodward *et al*[41]. It is promising that the potential of terahertz imaging technology as an *in vivo* tool for the study of skin hydration levels have enabled differentiation between diseased, normal and inflamed tissues [42]. In a similar way to how terahertz imaging could assist the planning of skin cancer surgery, Fitzgerald *et al*. have investigated the use of terahertz imaging to aid the removal of breast cancer intra-operatively[43].

Another potential application of THz imaging is the diagnosis of dental caries[44]. Caries are a result of mineral loss from enamel, and this causes a change in refractive

index within the enamel. Furthermore, there has been a strong drive in the pharmaceutical industry for comprehensive quality assurance monitoring and researchers have already started using TPI for this application[8].

1.2.3 THz Spectroscopy

A distinct advantage of terahertz imaging over other techniques is its ability to provide spectral information. The spectral information can be acquired by a Fourier Transform (FT) of the time domain THz waveform, as is done in Terahertz TDS. Many materials show different spectral fingerprints in the THz frequency range, which means that THz spectroscopy can be used for material identification. Therefore, time domain spectroscopy has been used to investigate tissue differentiation[45] by revealing their spectral properties over the THz regime.

1.3 Objectives

Terahertz imaging as a novel tool for medical applications is a recently emerging field and it has not been explored much compared with other conventional modalities. Therefore, the goal of this thesis is to facilitate TPI for future clinical use and the main work of this thesis will focus on the following aspects:

1. To develop new techniques that can be used to reveal the sample's structure and properties.

2. To develop a reliable protocol for both *ex vivo* and *in vivo* THz experiments to use in medical diagnosis.

1.4 Structure of this thesis

Chapter 2 shows the theory and technique as to how we do the de-noising process and extract the spectroscopy information (both frequency dependent refractive index (RI) and absorption coefficient (AC)) of measurement samples by using the time domain scanning. Also we will give a detailed description of the generation and

detection THz pulse and the configuration of our experimental system as well as the raw data format and a self-developed user interface programme for handling and processing the raw measurement data.

Chapter 3 presents results of an *ex vivo* study of both healthy and diseased rat liver tissues. A brief introduction to liver cirrhosis, the protocol of sample preparation, the measurement process and the discussion are involved in this chapter.

Chapter 4 presents results of *in vivo* studies of both human skin in different levels of temperature and humidity. A brief introduction to human skin, the protocol of experiment and the discussion will be described in detail in this chapter as well.

Chapter 5 shows the impact of both Signal to Noise Ratio (SNR) and Dynamic Range (DR) of time domain data on calculated frequency dependent RI and AC.

Chapter 6 gives a conclusion and a plan for future work

Chapter 2 Theory and experimental system

2.1 Theory
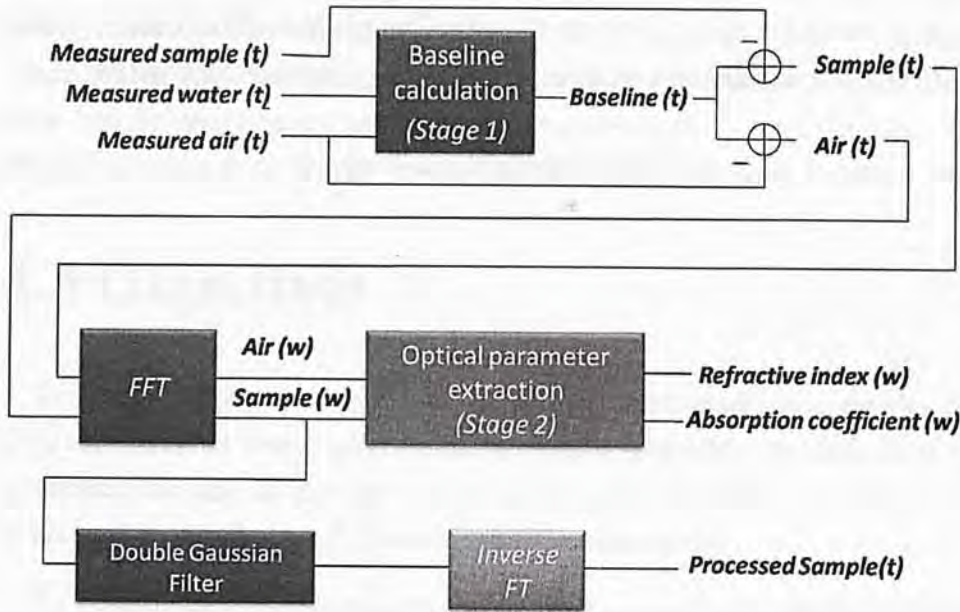
Figure 2.1: Schematic diagram for the whole data processing. There are three main processes namely1. Baseline calculation (Purple box), 2. Optical extraction (Orange box), 3.Double Gaussian Filter (Red box).

In chapter 2, we discuss all the data processing techniques included in our work step by step. A block diagram for the whole process is illustrated in Figure 2.1. For every measurement, in addition to measuring the reflections off the tissue samples, we measured the empty window (namely the reflection off the quartz/air interface) and then a reflection of water. The air and water measurements were used to determine the baseline (see Section 2.1.3 Baseline calculation) namely any unwanted enduring reflections. The baseline was then

subtracted from the air and sample measurements and these resulting waveforms would undergo Fourier Transformation (FT) and then a calculating process to obtain the frequency dependent RI and AC of the samples (see Section 2.1.4). At the same time, we would employ the Double Gaussian Filter (DGF) (see Section 2.1.3 Baseline calculation) on the baseline-subtracted sample waveform in the frequency domain. Finally we can get a filtered sample waveform in the time domain by doing the inverse FT on the raw sample waveform.

2.1.1 Propagation of electromagnetic field through dielectric media
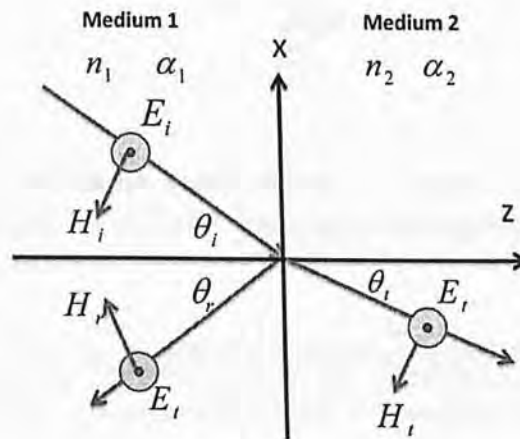
Figure 2.2: Schematic diagram of a transverse electromagnetic (TEM) wave move from medium 1 to medium2. Both directions of associated magnetic and electric field are indicated.n and α and represent the refractive index absorption coefficient of medium respectively.

Consider a transverse electromagnetic (TEM) wave propagating in the **z** direction where both the electric field E and magnetic field H are orthogonal to the direction of propagation. The electric field has frequency component ω and can be expressed in terms of separate time and spatial dependencies as:**Eq 2.1**

$$E_\omega(z, t) = E_{z=0}(\omega)e^{i(\omega t - k_z z)}$$

(Eq 2.1)

$E_{z=0}(\omega)$ is the initial amplitude of the electric field at particular frequency where k_z denotes the z component of frequency dependent complex wave vector k_i. It is related to the complex refractive index n by factoring k_0, the magnitude of wavevector in free space:

$$k_i = k_0 n$$

(Eq 2.2)

Alternatively we can extract refractive index $n_i(\omega)$ and absorption coefficient $\alpha_i(\omega)$ by wave vector k_i (Eq 2.3).

$$k_i(\omega) = \frac{\omega}{c} n_i(\omega) - \frac{i}{2} \alpha_i(\omega)$$

(Eq 2.3)

Both reflection and refraction occur at the interface when a THz wave propagates into a media with different refractive index as showing in Figure 2.2 where θ_i, θ_r and θ_t are the angles of incident, reflection and refraction respectively and $\theta_i = \theta_r$. We choose the direction of the interface in the x-y plane (the plane z=0) and define the electric field to be polarized along the y direction which means the wave is S-polarized. According to the boundary conditions derived from the Maxwell equations applied at the interface between two dielectric media, the tangential components of **E** and **H** with the same frequency are continuous across the interface and yield the following equations:

$$E_i(\omega) + E_r(\omega) = E_t(\omega)$$

(Eq 2.4)

$$H_i(\omega) \cos \theta_i - H_r(\omega) \cos \theta_i = H_t(\omega) \cos \theta_t$$

(Eq 2.5)

And by Maxwell equation we can get the following equation:

$$H_y(\omega) = \frac{k}{\mu\omega} E_x(\omega) = \frac{1}{\eta} E_x$$

(Eq 2.6)

$$k = \omega\sqrt{\mu\varepsilon}$$

(Eq 2.7)

$$\eta = \sqrt{\mu/\varepsilon}$$

(Eq 2.8)

By rearranging the **Eq 2.4** to **Eq2.8**, Fresnel equation (complex reflectivity R) can be obtained as

$$R = \frac{E_r(\omega)}{E_i(\omega)} = \frac{k_{medium1}(\omega)\cos \theta_i - k_{medium2}(\omega)\cos \theta_t}{k_{medium1}(\omega) \cos \theta_i + k_{medium2}(\omega) \cos \theta_t}$$

(Eq 2.9)

2.1.2 A de-noising method
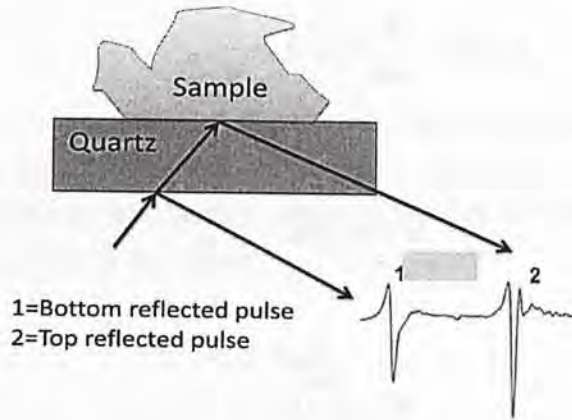
Figure 2.3: Schematic diagrams to illustrate physical measurement (with non air sample) interface and the respective reflected waveform. Pulse 1 and Pulse 2 represent the bottom and top quartz reflection respectively.

In our system, all the samples of the measurements are placed on a quartz window topped with the scanning area. The detailed configuration will be discussed in section 2.2. The terahertz radiation is focused onto the top surface of the window.

As the incident THz pulse propagates through the quartz window, the reflected signal will contain two reflections, namely the reflected pulse from the bottom and top of the quartz window shown in Figure 2.3. The "bottom" reflected pulse is named "baseline". Clearly, only the "top" reflected pulse includes sample information. So our aim is to filter out the baseline from the collected data. "Bottom" reflected pulse has an enduring signal or "ringing" which will extend into the "Top" reflected pulse. Due to this overlapping, the tail cannot be measured directly. To tackle this problem, our group has developed a method to determine the baseline offset through water measurement[46]. The detail of this method is described in detail in Section 2.1.3.

Here we outline a de-noising (to cancel the baseline) process. Let us assume $E_{sample}(t)$ to be the measured raw pulse from a sample and $E_{baseline}(t)$ to be

the baseline measurement, and then the actual reflected pulse carrying the sample features is:

$$E_{actual}(t) = E_{sample}(t) - E_{baseline}(t)$$

<div align="right">(Eq 2.10)</div>

The shape of a THz pulse is quite complicated to be determined when the reflections take place within a sample. A reference measurement $E_{reference}(t)$ is taken in order to extract the impulse function and remove the system variability. This reference measurement is generally taken with nothing on the quartz window, (i.e.to measure the reflection of air). The de-noising process is therefore first to subtract the baseline from the sample and reference waveforms to remove irrelevant reflections. Next, the sample waveform is divided by the reference waveform in frequency domain to remove the system response and leave only the impulse function of the sample. The required frequency spectra are obtained by the following equation.

$$FT(impulse function) = FT(filter)X \frac{FT\left(E_{sample}(t) - E_{baseline}(t)\right)}{FT\left(E_{reference}(t) - E_{baseline}(t)\right)}$$

<div align="right">(Eq 2.11)</div>

Dividing the sample by the reference removes the dependence of the shape of the THz pulse but also increases the noise. In this work a DGF function is applied to remove both the low and high frequency noise components and also to produce a suitable time domain response.

The form of the filter in the time domain is expressed in **Eq 2.12**. Where **h** and **l** are the high and low pass filter settings which determined the band pass of the filter. The band pass filter is adjusted to match the bandwidth of the sample THz pulses so as to remove any out-of-band noise and anomalies arising from deconvolution. t_o determinates the peak location of the filter in the time domain. In the frequency domain t_o dictates how well the out-of-band noise is

suppressed. For the best suppression of out-of-band noise, t_o is set at the center point on the time axis. The DGF function was selected carefully so that the sample features could still be resolved. If too many of the high frequency components were filtered out, we could not resolve the two reflection pulses from the sample. After finishing all the process about **Eq 2.11**, by doing the inverse Fourier Transform (FT^{-1}), an actual and processed time domain sample waveform can be obtained (see **Eq 2.13**).

$$filter = \frac{1}{h}\exp\left(\frac{-(t-t_o)^2}{h^2}\right) - \frac{1}{l}\exp(\frac{-(t-t_o)^2}{l^2})$$

(Eq 2.12)

$$E_{actual}(t) = FT^{-1}\left(FT(impulse function)\right)$$

(Eq 2.13)

2.1.3 Baseline calculation

In order to cancel the effect of baseline, our group has already developed a reliable and accurate baseline estimation method[46]which is to use accurate, room temperature, Terahertz Pulsed Transmission Spectroscopy (TPS) data of a standard material such as water to simulate the reflected terahertz pulse for a given input pulse.

In our calculations we use the measured reference pulse (air reflection) in conjunction with a measured frequency dependent optical properties of water and Fresnel equations to predict the reflection off water. We chose water for this as it will naturally make perfect contact with the quartz window. By comparing the simulated water reflection with the measured water reflection, the effect of the ringing (unwanted signal) can be determined and this ringing can then be accounted for in calculations of unknown samples such that the optical properties of these samples can be determined more accurately.

Each measured electric field is the superposition of the actual reflection due to the interface with the baseline reflection (**Eq 2.14-2.15**)

$$E_{air}^{mea}(t) = E_{air}^{act}(t) + E_{baseline}^{sim}(t)$$

(2.14)

$$E_{water}^{mea}(t) = E_{water}^{act}(t) + E_{baseline}^{sim}(t)$$

(2.15)

If we assume the measured sample is homogenous, the THz radiation of every measurement can be presumed to be a result of its interaction with only two kinds of mediums (i.e that of the quartz and the measuring sample). With reference to **Eq 2.9,** we can write down the complex reflectivities of the quartz/air interface R_{air}^{quartz} and quartz/water interface R_{water}^{quartz} i.e

$$R_{air}^{quartz}(\omega) = \frac{E_{air}(\omega)}{E_{incident}(\omega)} = \frac{k_{quartz}(\omega)\cos\theta_{quartz} - k_{air}(\omega)\cos\theta_{air}}{k_{quartz}(\omega)\cos\theta_{quartz} + k_{air}(\omega)\cos\theta_{air}}$$

(2.16)

$$R_{water}^{quartz}(\omega) = \frac{E_{water}(\omega)}{E_{incident}(\omega)} = \frac{k_{quartz}(\omega)\cos\theta_{quartz} - k_{water}(\omega)\cos\theta_{water}}{k_{quartz}(\omega)\cos\theta_{quartz} + k_{water}(\omega)\cos\theta_{water}}$$

(2.17)

Where, $k_j(\omega) = \frac{\omega}{c}n_j(\omega) - \frac{i}{2}\alpha_j(\omega)$ is the frequency dependent complex refractive index of a medium with refractive index **n** and absorption coefficientα and **c** is the speed of light in vacuum ($3\times10^8 ms^{-1}$). The angle of incidence of the light entering the quartz is θ_{quartz}, and the angles of refraction in air and water are θ_{water} and θ_{air}respectively. Values for k_{air} and θ_{air} are known. Spectroscopy data acquired in transmission geometry are used for calculating $k_{quartz}$and k_{water}.By dividing the above two equations with each other, the term $E_{incident}(\omega)$ iseliminated to give a ratio **M** in the frequency domain which relates the actual air reflection $E_{air}(\omega)$and actual water reflection $E_{water}(\omega)$.

$$M = \frac{E_{water}(\omega)}{E_{air}(\omega)}$$

$$= \left(\frac{k_{quart}(\omega)\cos\theta_{quartz} - k_{water}(\omega)\cos\theta_{water}}{k_{quart}(\omega)\cos\theta_{quartz} + k_{water}(\omega)\cos\theta_{water}}\right)\left(\frac{k_{quart}(\omega)\cos\theta_{quartz} + k_{air}(\omega)\cos\theta_{air}}{k_{quart}(\omega)\cos\theta_{quartz} - k_{air}(\omega)\cos\theta_{air}}\right)$$

$$(2.18)$$

The angles θ_{water} and θ_{quartz} can be calculated from Snell's law:

$$n_{quartz}\sin\theta_{quartz} = n_{water}\sin\theta_{water} = n_{air}\sin\theta_{air}$$

$$(2.19)$$

From **Eq 2.3, Eq 2.15, Eq 2.18** and **Eq 2.19**, we obtain the following formula for $E^{sim}_{baseline}(\omega)$:

$$E^{sim}_{baseline}(\omega) = E^{mea}_{water}(\omega) - E^{act}_{water}(\omega)$$

$$= E^{mea}_{water}(\omega) - ME^{act}_{air}(\omega)$$

$$= E^{mea}_{water}(\omega) - M[E^{mea}_{air}(\omega) - E^{sim}_{baseline}(\omega)]$$

$$= \frac{E^{mea}_{water}(\omega) - ME^{mea}_{air}(\omega)}{1 - M}$$

$$(2.20)$$

The simulated $E^{sim}_{baseline}(t)$ can then be calculated by taking the inverse FT of $E^{sim}_{baseline}(\omega)$. This simulated baseline is then used to calculate the actual reflected pulse:

Figure 2.4: Schematic diagram to illustrate the raw data of Air (Blue solid line), Sample (Black solid line) and the calculated Baseline (Red solid line) on the domain.

$$E^{act}(t) = E^{mea}(t) - E^{sim}_{baseline}(t)$$

(2.21)

The actual electric field is then used to obtain the complex refractive index of a test material. The detailed calculation will be discussed in the following section.

2.1.4 Frequency-dependent Refractive Index and Absorption Coefficient
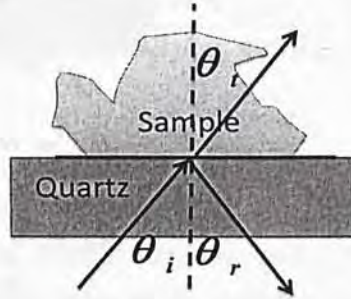
Figure 2.5: Schematic diagram to illustrate physical measurement. All incident, transmission and reflection pulses are shown.

As we have mentioned many times, TPI can obtain both the amplitude and phase information of the detected THz waves in the frequency domain. Therefore, the RI $n_c(\omega)$ and AC $\alpha_c(\omega)$ of a sample can be acquired through

the Fresnel coefficient in a reflection mode. And we can link them up by **Eq 2.3** which is a function of frequency (ω) such that $k_j(\omega){=}\frac{\omega}{j}n_c(\omega)-\frac{i}{2}\alpha_j(\omega)$. In the remainder of this section, a detailed explanation on how the complex refractive index is calculated in our system geometry will be given.

The zero value of the angle of incidence (i.e $\theta_i = \theta_t = \theta_r = 0$)in the normal incidence geometry enables analytical extraction of the complex refractive index, whereas in the non-normal case things become complicated due to the involvement of the angles $\theta_i \neq 0$, as shown in Figure 2.5

Once we want to extract the optical parameters of the sample, beside the reflection of sample, we have also to measure the reflection of air (shown in Figure 2.6).

$$\theta_i = \theta_{quartz}$$
$$\theta_t = \theta_{sample}$$
$$\theta_i = \theta_r$$

(a)

$$\theta_i = \theta_{quartz}$$
$$\theta_t = \theta_{air}$$
$$\theta_i = \theta_r$$

(b)
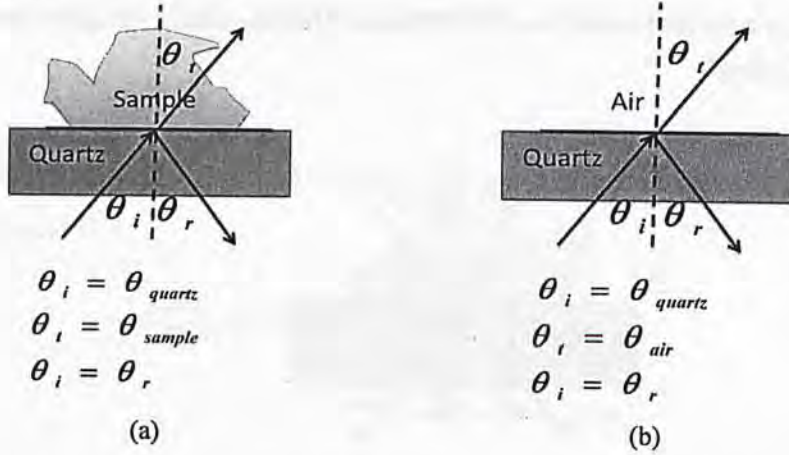
Figure 2.6: Schematic diagrams to illustrate physical measurement with (a) sample (b) air (or so called reference). All the values of different angles were specified.

With reference to **Eq 2.9** and the configuration of Figure 2.6, we can write down the complex reflectivities of the quartz/air interface R_{air}^{quartz} and quartz/sample interface R_{sample}^{quartz} i.e

$$R_{air}^{quartz}(\omega) = \frac{E_{air}(\omega)}{E_{incident}(\omega)} = \frac{k_{quart}(\omega)\cos\theta_{quartz} - k_{air}(\omega)\cos\theta_{air}}{k_{quart}(\omega)\cos\theta_{quartz} + k_{air}(\omega)\cos\theta_{air}}$$

(2.22)

$$R_{sample}^{quartz}(\omega) = \frac{E_{sample}(\omega)}{E_{incident}(\omega)} = \frac{k_{quart}(\omega)\cos\theta_{quartz} - k_{sample}(\omega)\cos\theta_{sample}}{k_{quart}(\omega)\cos\theta_{quartz} + k_{sample}(\omega)\cos\theta_{sample}}$$

$$(2.23)$$

And by combing the **Eq 2.22 and Eq 2.23** we canget ratio of $E_{sample}(\omega)$ and $E_{air}(\omega)$ i.e

$$\frac{E_{sample}(\omega)}{E_{air}(\omega)}$$

$= R$

$$= \left(\frac{k_{quart}(\omega)\cos\theta_{quartz} - k_{sample}(\omega)\cos\theta_{sample}}{k_{quart}(\omega)\cos\theta_{quartz} + k_{sample}(\omega)\cos\theta_{sample}}\right)\left(\frac{k_{quart}(\omega)\cos\theta_{quartz} + k_{air}(\omega)\cos\theta_{air}}{k_{quart}(\omega)\cos\theta_{quartz} - k_{air}(\omega)\cos\theta_{air}}\right)$$

$$(2.24)$$

Again, **Eq 2.24** can be rearranged. However, this time rather than k_{sample} only the product $k_{sample}\cos\theta_{sample}$ can be extracted.

$$k_{sample}\cos\theta_{sample} = \frac{(1-R)k_{quartz}^2\cos^2\theta_{quartz} + (1+R)k_{quartz}\cos\theta_{quartz}k_{air}\cos\theta_{air}}{(1-R)k_{air}\cos\theta_{air} + (1+R)k_{quartz}\cos\theta_{quartz}}$$

$$(2.25)$$

Since all the values in the right side of **Eq 2.25** are either known or can be obtained from recorded signals, now the question becomes how to solve $\cos\theta_{sample}$. From Snell's law, we know that this angle is actually dependent on the refractive index of the medium where the light propagates. In our system, we can get their relation as,

$$n_{quartz}\sin\theta_{quartz} = n_{sample}\sin\theta_{sample}n_{air}\sin\theta_{air} = 1 * \sin 30° = \frac{1}{2}$$

$$(2.26)$$

And let

$$k_{sample} \cos \theta_{sample} = Z$$

(2.27)

and take real parts of both sides we can obtain

$$n_{sample} \cos \theta_{sample} = Re(Z)$$

(2.28)

Using **Eq 2.26** and **Eq 2.28**, $\cos \theta_{sample}$ can be expressed as,

$$\cos \theta_{sample} = \frac{Re(Z)}{\sqrt{\frac{1}{4} + (Re(Z))^2}}$$

(2.29)

Then substitute **Eq 2.29** into **Eq 2.25** and we can obtain k_{sample}. Meanwhile, the frequency dependent refractive index and absorption coefficient can also be determined as

$$n_{sample} = \frac{Re(Z)}{\cos\theta_{sample}}$$

(2.30)

$$\alpha_{sample} = -\frac{2\omega}{c} \frac{Im(Z)}{\cos\theta_{sample}}$$

Where c is the speed of light

(2.31)

2.2 Experimental Configuration

In this work, the system we used for experiments employ photoconductive antennas to generate and detect the terahertz radiation. After this section, you are supposed to have understood the whole picture of the mechanism of Terahertz generation and detection inside our system. Also you can have a deeper view of the characteristics of the terahertz waveform generated by our system which would definitely help you understand the following chapters. Both the power spectrum and time domain performance of the emitted waveform will be shown later on in this section.

2.2.1 Terahertz generation and detection

Two decades ago, as the THz sources at that time were still expensive, bulky and inefficient, which really prevented scientists and scholars from having a further research and development of THz, Therefore the advancement of ultrafast technology for generating and detecting coherent THz rays clearly is a catalyst for speeding up the development the THz technology. The current THz emitters include free electron lasers which can provide high THz power up to 20W on average [47]; electronic emitters such as Gunn diode, Bloch oscillator, cold plasma; Semiconductor THz laser [48]; and the dominating method is utilizing photoconductive dipole antenna or electro-optic crystal by focusing mode-locked femtosecond pulsed laser on them.
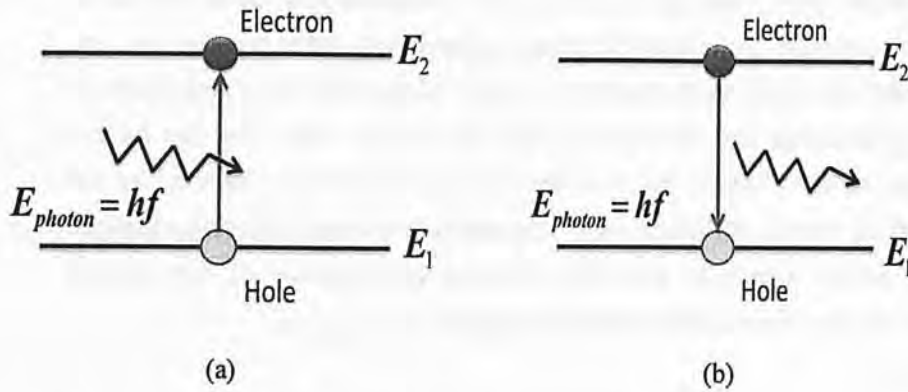
Figure 2.7: Schematic diagrams to illustrate that (a) the generation an electron –hole pair excited by an electromagnetic wave (photon) and (b) the generation of electromagnetic wave (photon) excited by a recombination of an electron –hole pair.

The generation of THz pulse with photoconductive antenna makes use of the physics of electron-hole pair recombination (shown in Figure 2.7). A laser pulse with photon energy $E_{photon} = hf$ greater than the energy bandgap of the material $E_2 - E_1$ being excited is required to generate the electron hole pairs. Conventionally, photoconductive antenna is generally made of gallium arsenide (GaAs) or low temperature grown GaAs (LT-GaAs). The energy bandgap of GaAs is about 1.42eV. To fulfill the excitation requirement, the wavelength of the laser pulse must be shorter than $873nm (E_{photon} = hf = \frac{hc}{\lambda} \geq 1.42eV)$.

Hence, in our THz radiation generation, an 800nm laser pulse is employed in our experiment to excite a GaAs photoconductive antenna.

Electron hole pairs are created and accelerated towards the electrodes in opposite directions with the presence of the applied electric field. The emitted terahertz field is therefore contributed and dominated by the ultra-fast change of carrier density at the instant the laser pulse arrived. Meanwhile, the rapid acceleration of the carriers also accounts for the generated THz field. **Eq 2.32** describes the above relationship.

$$E_{THz} \propto \frac{dj}{dt} = \frac{d}{dt}(nev) = \frac{dn}{dt}ev(t) + n(t)e\frac{dv}{dt}$$

<div align="right">(2.32)</div>

where j is the current density, n is the carrier number density and v is the carrier drift velocity. The carrier number density depends on the power of incident laser radiation. The carrier drift velocity v depends on the applied electric field. This means that besides the response characteristics of the antenna, the strength of the THz field is determined by the laser power and the applied field voltage.
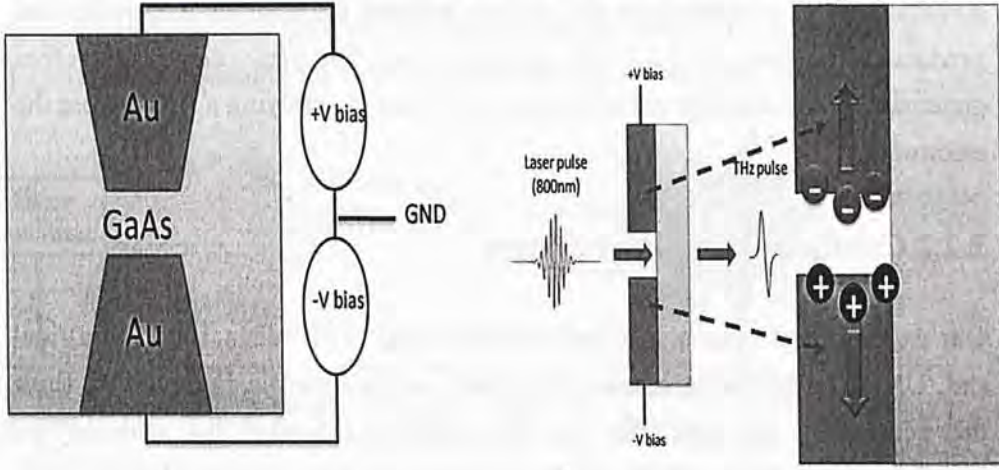
Figure 2.8:(Left) A diagram shown a bow tie photoconductive antenna with gold electrodes attached on a GaAs substrate with bias (Front view). (Right) A schematic diagram of THz emission due to the excitation of electrons with a GaAs substrate (Side view).

Figure 2.8 illustrates the schematic diagram of THz emission due to excitation of electron hole pairs within a GaAs substrate. Gold electrodes with a bow-tie structure are attached on the substrate for applying the bias voltage. The bow-tie structure is used as it has a broadband response. Ti: sapphire laser is the most common candidate to provide femtosecond pulses with 800nm wavelength. The pump beam is focused onto the photoconductive switch. When the central gap of the biased switch is illuminated by femtosecond laser pulses,

photo-excited carries are accelerated and create an ultra-short current. The relaxation of these carriers produces a broad band terahertz field.

Similarly the THz detection we employed is attained by another identical photoconductive dipole antenna in the reverse mechanism of THz generation. A femtosecond pulse, which is derived from the laser beam used for THz generation at the same time, hits on the photoconductive antenna and excites the electron hole pairs on the substrate. When a THz pulse reaches the antenna simultaneously, it accelerates the carriers towards the antenna electrodes and produces a transient current in the detector circuit. The bias voltage is therefore generated by the detected electric field rather than by applying a field across the electrodes.

2.2.2 Configuration of our system

Our experimental system is a commercial imager, TPI Imaga 1000 (TeraView Ltd, UK). The hardware schematic diagram is illustrated in Figure 2.10. Both the generation and detection for the terahertz radiation are achieved by low-temperature-grown GaAs photoconductive devices and an ultrafast laser (Vitesse, Coherent Inc.), emitting 90 fs pulses centered at a wavelength of 800 nm, with a 80 MHz repetition rate and an average power of about 200 mW.
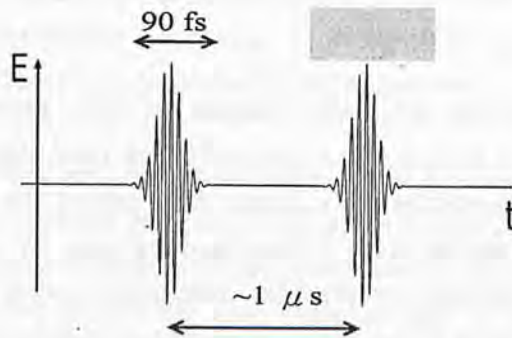
Figure 2.9: A schematic diagram of the pulsed laser output (not in scale)

The laser beam is separated into the pump and probe beams by a beam splitter. The pump beam is focused onto the photoconductive switch. After the electron

hole-pair recombination discussed in previous section, a broad band terahertz radiation can be obtained. The emitted terahertz waves are then focused onto the sample by a silicon lens and a pair of Off-Axis Parabolic (OAP) mirrors.

In the detection branch, the terahertz pulses reflected off the sample are re-collimated using another pair of off-axis parabolic mirrors and focused onto the photoconductive receiver. Rather than applying a biased voltage to the electrodes, the laser pulse is employed to gate the switch, and a current amplifier and ammeter are connected to measure the transient current generated by the laser pulse and the THz electric field. The measured current is directly proportional to the time varying electric field of the THz radiation. In this way, both the amplitude and phase of the incident THz wave can be obtained by sweeping the optical delay through the entire terahertz pulse (at for instance a rate of 15 Hz) thus obtaining the time-domain terahertz waveforms.
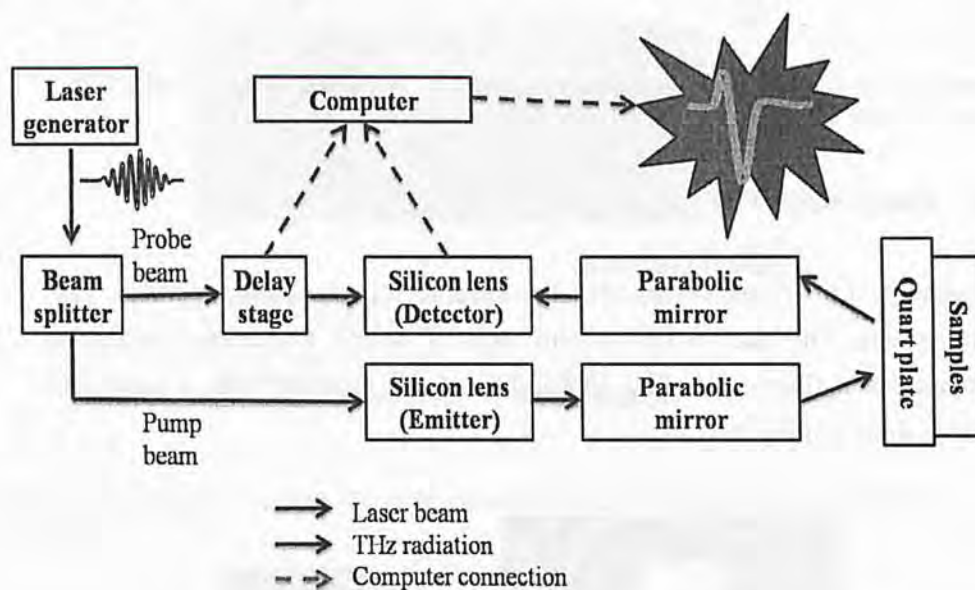
Figure 2.10: Hardware block diagram of our group TPI system.

(a) (b)
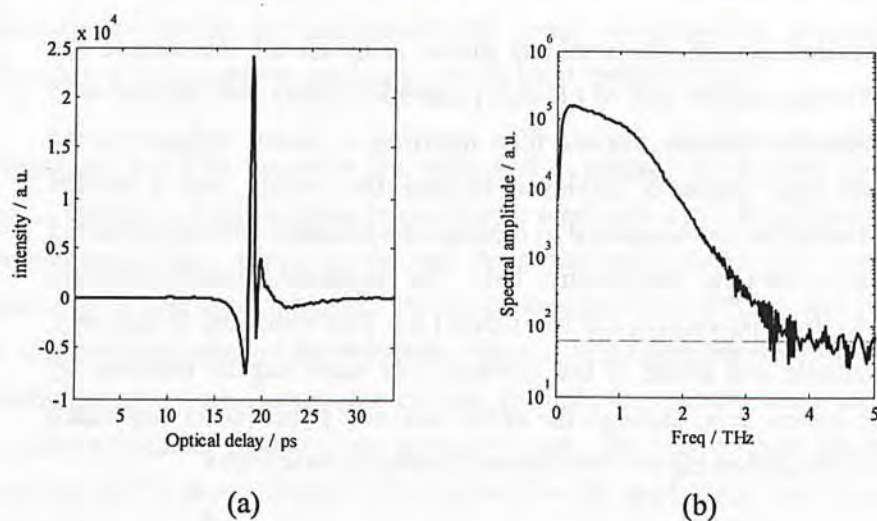
Figure 2.11: (a) Temporal waveform of a mirror sample (b) The corresponding spectrum with mean noise level.

2.2.3 Hand-held TPI Setup

TeraView Ltd. (Cambridge, UK) has recently developed a handheld THz probe system. The laser in this system used for optical excitation reaches the antennas via a fiber optic. The appearance of the machine with a hand-held probe is shown in Figure 2.12.
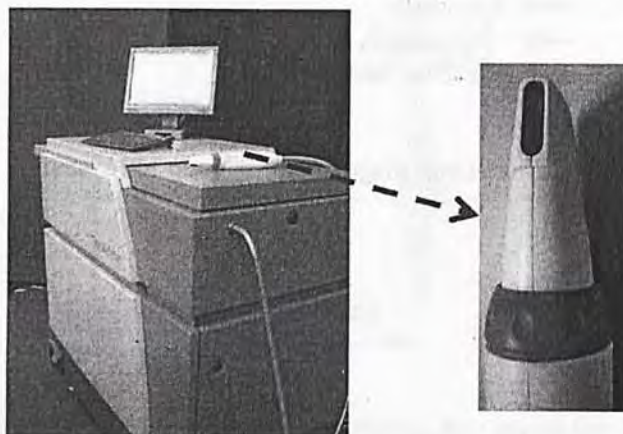
Figure 2.12: The overview of the experiment system

The probe is used to contact the sample directly with an angle of incidence of $3.48°$ (this angle is non-adjustable) and the reflected terahertz pulse from the quartz/sample interface is detected coherently. The THz beam is scanned up and down across the center line of the window to form a line scan. The scanning motion is achieved by controlling a Risley prism beam steering system, which includes a pair of Risley prisms and a set of motors and bearings as seen in the Figure 2.13[49] Consider the case of only one wedge prism, when the prism rotates, the steering beam travels in a circle along the optical axis. When two wedge prisms aligned and rotated together, the output beam is the superposition of the circles resulted from two prisms rotating independently. Hence, by matching wedge prisms with different wedge angles and controlling the rotating speed of the two prisms, the steering beam would result in different scanning patterns.
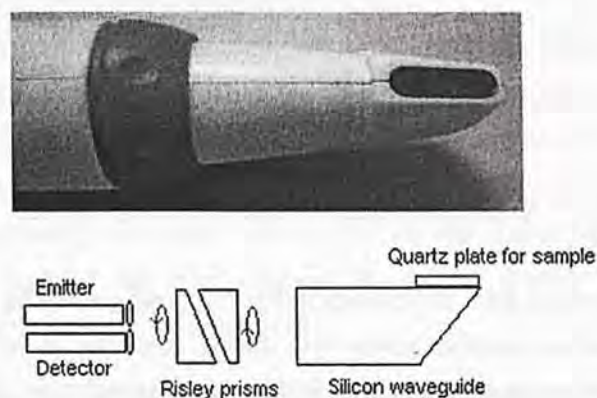
Figure 2.13: (Upper) A close view of the hand-held probe and (Lower) a schematic of the probe.

In the case of our probe, a line scanning pattern is achieved by rotating the two prisms with the same wedge angles in opposite directions, given the initial orientations are identical for two prisms. The scan speed of the system is up to 8 lines per second. The scan length is 8 mm and each line contains at most 25 pulses, so it means at most 200 pulses per second. The usable frequency range is from about 0.1 THz to 1.6 THz but the valid range tends to decrease when the sample is in an aqueous phase due to signal attenuation by the sample. Terahertz spectroscopy is typically done with an average point measurement of

a homogenous sample and the resulting terahertz electric field can be recorded as a function of time.

2.3 Data Structure

	Line_Numb...	Pulse_Num...	Line_Directi...	Pulse_Dire...	Pulse_Angle	Pulse_Data
0	0	0	0	1	355.87448	253.43419, 254.52797, 251.27126, 250.77069, 253.47078, 252.85094, 2...
1	0	1	0	0	2.7735806	251.90742, 255.23866, 256.93564, 253.51529, 252.9935, 253.34596, 25...
2	0	2	0	1	9.67268	250.82387, 253.01698, 255.63597, 253.07825, 251.12021, 254.43233, 2...
3	0	3	0	0	16.57178	253.08334, 255.14423, 257.14978, 252.67741, 249.16182, 254.01358, 2...
4	0	4	0	1	23.470879	253.23032, 251.7322, 251.53339, 250.40784, 251.28572, 252.14569, 25...
5	0	5	0	0	30.369978	249.11154, 249.37654, 255.18358, 251.54655, 250.58963, 252.82347, 2...
6	0	6	0	1	37.269077	246.42958, 249.81258, 251.49057, 250.35632, 248.2903, 251.43231, 25...

Table 2.1: The structure of the raw data with HDF5 format.

Table 2.1 demonstrates how the collected data are arranged in the HDF5 file. The THz beam position on the center line during scanning is recorded and represented by the prism rotation angle; it is the term "Pulse Angle" listed in the table (from $0°$ to $359°$). We would use 6 kinds of data parameters to define a particular pulse. The 6 kinds of data are 1.Line_Number 2.Pulse_Number 3.Line_Direction 4.Pulse_Direction 5.Pulse_ Angle and 6.Pulse_Data.

The THz beam scans up and down at the center line of the probe. The longer the measurement, the more lines of data are recorded; each pulse has a corresponding line number. The up and down directions are indicated by the "0" and "1" in the column "Line Direction". It records about 26 point-measurements along a line scan. The pulse number is listed on the column "Pulse Number" counted from 0 to 25. And the pulse direction changes one after one as indicated by the "0" and "1" in the column "Pulse Direction". The pulse number recounts again from zero for another line. The pulse waveform data of each point measurement is shown on the last column named "Pulse Data". There is a tiny change of the amplitude and phase between the pulses at different locations. For each "Pulse Data" cell we have 256 points of data.

2.4 Pre-processing and the user interface

2.4.1 Data pre-processing 1 (Chopping)

As we mentioned in section 2.2.1, every reflection Terahertz pulse generated by our reflection system gives two reflections called 'top' reflection and 'bottom' reflection from the quartz plate. But only the top reflection contains interesting information from the samples. Therefore before doing the baseline calculations, Double Gaussian filtering and optical parameters extraction we have to do the chopping to cancel the effect from the quartz bottom reflection for avoiding from data contamination.

Ideally, for different measurements we should get the exactly the same quartz bottom reflection but in reality we found that there would be a slight difference between them. For the sake of comparison and consistency among the different measurement of same sample, we suggest to do the alignment before those processing discussed before. For all the measurement we did, "Least Square" method has been chosen to do the bottom quartz pulse reflection alignment (shown in Figure 2.14).

Normally we can use the midpoint of the data as a benchmark to classify the 'top' reflection (after benchmark) and 'bottom' reflection pulses (before the benchmark). But sometimes we have to do several ten points shifting for the separating (either towards left or right). After the identifying the benchmark, we would use the bottom reflection pulse from the water measurement as a "Least Square" alignment reference. Finally, by doing the removal of first pulse to each data set we can get the wanted sampled pulses from the measurements.

Step 1: (raw data)	E_{water}^{meas} E_{sample}^{meas} E_{air}^{meas}
Step 2: (Least Square Alignment)	E_{water}^{meas} E_{sample}^{meas} E_{air}^{meas}
Step 3: (Quartz bottom pulse Separation)	E_{water}^{meas} E_{sample}^{meas} E_{air}^{meas}
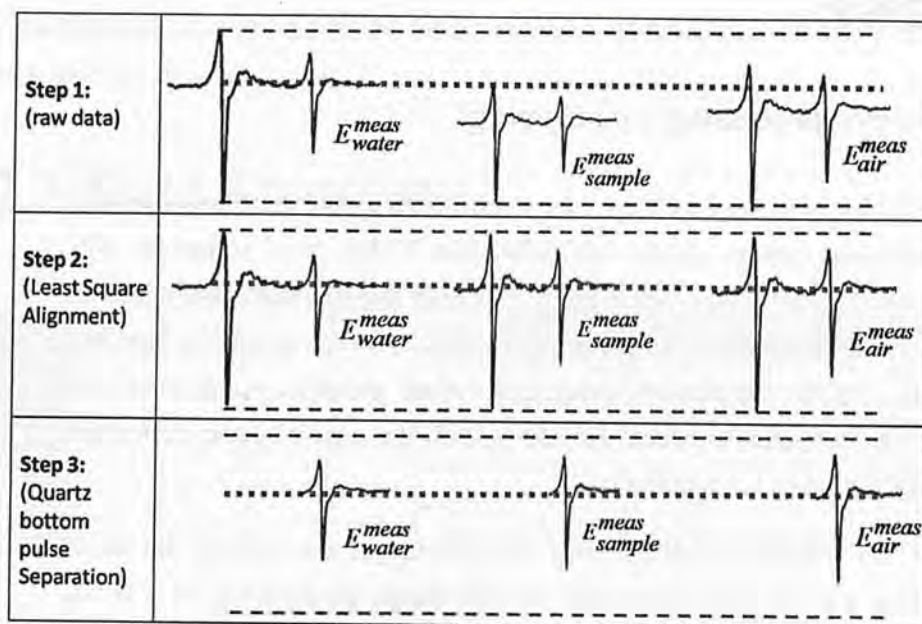
Figure 2.14: Pre-processing operation (Chopping). Step 1: get the raw data, Step 2: conduct "least Square" alignment, Step 3 conduct the quartz bottom pulse separation.

2.4.2 Data pre-processing 2 (Angle selection)

According to section 2.3 we know that there is column to save the angles of the pulses in the resulted HDF5 document. And after our quantitative studies, for each measurement, we found only a specific range of angles whose data contain information we wanted and it is due to the rotation of the prism inside the machine and the non-matching between quartz plate area and scanning area. We found that we can only get the response as long as we place the sample in the middle of the quartz plate called effective area. Therefore during the measurement we would make sure the sample completely cover the effective area (8mm x 5mm) (shown in Figure 2.15). And for the sake of the accuracy of data analysis, besides chopping, we have to do the data selection before we do the baseline calculations, Double Gaussian filtering and optical parameters extraction.

By showing all the pulses along all the angles (shown in Figure 2.16) we can see the problem of scanning area non-matching clearly. We found that only the pulses inside the middle range of angle (the purple circle). Otherwise, those

pulses did not contain any information we need. For the sake of the reliability of the data analysis, we would show all the pulses of the measurement along the full angle range, and then we would do the data selection manually such that selecting the effective angle range for the next step processing.
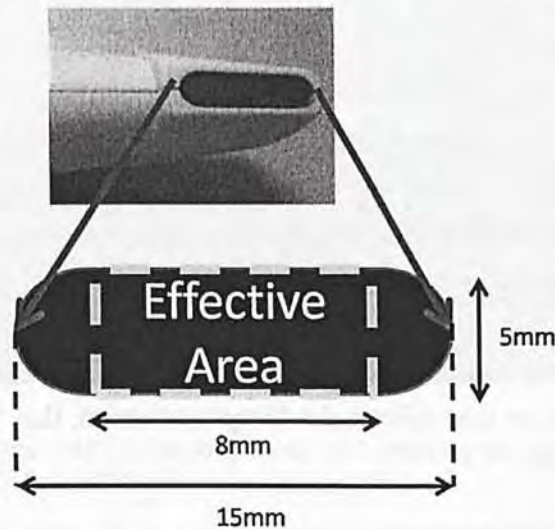
Figure 2.15: A schematic shown the effective measurement area of the probe
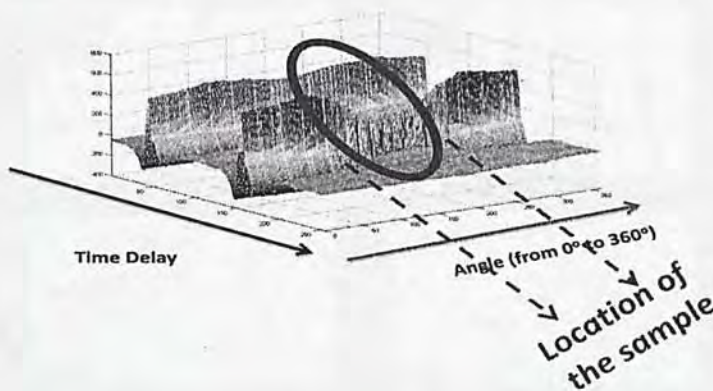
Figure 2.16: A 3D plot shows all the reflection pulses arranged along with angle (from 0o to 360o) within the same measurement. The purple ellipse emphasizes the wanted and correct pulses.(useful pulses)

2.4.3 The user interface for the data processing

For the sake of the analysis, a tailor-made Matlab programme for the data processing have been designed. Under the development of that besides the accuracy, usability is also an important consideration. Figure 2.17 shows the programme's interface. In addition to the baseline calculation, Double Gaussian Filtering and optical parameters extraction, the programme can also perform the "Chopping" and "Angle selection" which discussed before. Meanwhile in order to adapt different users' interpolation habit, interpolation function in the user interface is provided which can provide three different size interpolations (256, 512 and 1024). As long as user follows the "Step" indication, they will get all the calculations I provide.

P.S: A user interface for analyzing the terahertz time domain measurement for flat-bed system is also developed (see Figure 2.18)
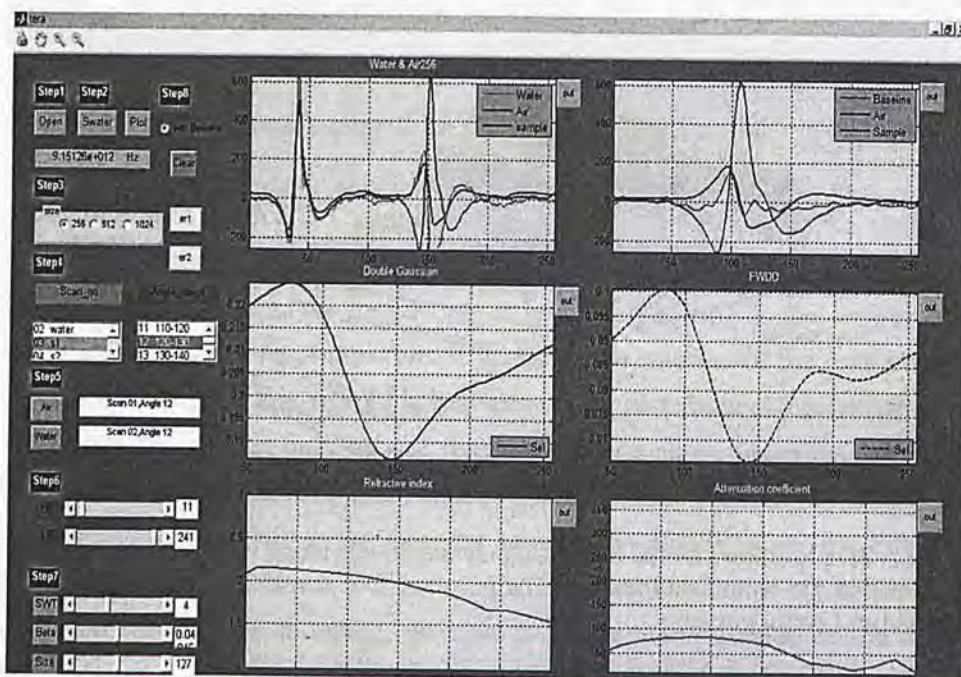
Figure 2.17: My own Matlab based graphic user interface for data analysis. All the provided functions are located in left side of the interface and the right side of it display all the respective calculated result.
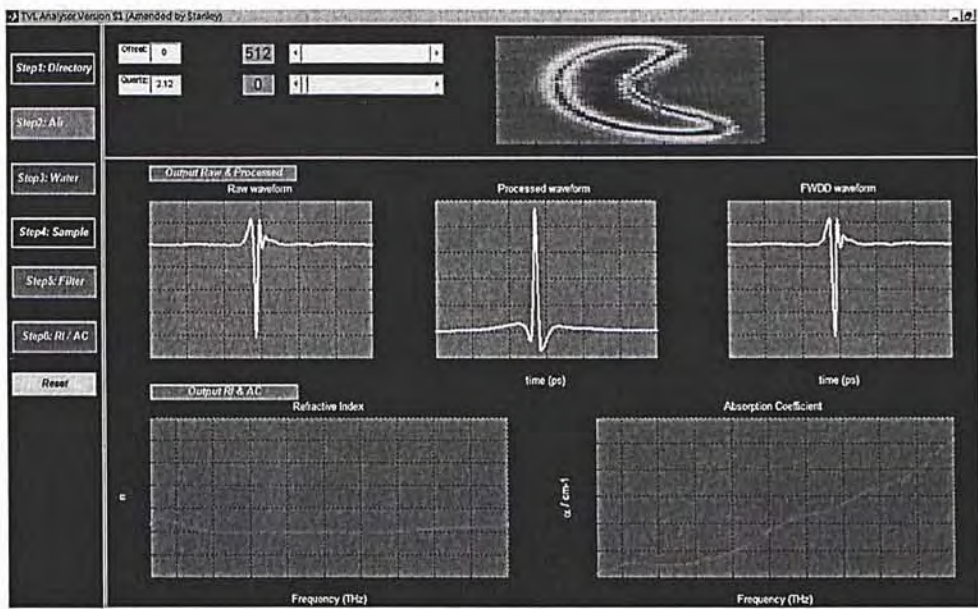
Figure 2.18: Another Matlab based graphic user interface designed by me for data analysis for using "flat-bed" Terahertz scanning system

Chapter 3 Ex-*vivo* experiment: investigating the origin of contrast

As we mentioned in Chapter 1, in this thesis we would use both *ex vivo* and *in vivo* experiments using TPI technique for exploring the medical potential of terahertz. For *ex vivo* experiment we chose rat liver cirrhosis to be our study target. In this chapter we will give the details of the experiment such as sample preparation, experimental protocol, how the result is calculated and a novel method to investigate different tissue structures.

3.1 Liver Cirrhosis

3.1.1 Liver

The liver is an important organ in the body. There are two main critical functions it performs; to produce substances required by the body and to remove toxic substances that can be harmful to the body, for example, drugs. The liver also has an important role in regulating the supply to the body of glucose and lipids that the body uses as fuel. In order to perform these critical functions, liver cells must be working normally, and they must have an intimate relationship with the blood since the substances that are added or removed by the liver are transported to and from the liver by the blood.

3.1.2 Liver cirrhosis

Liver cirrhosis is a complication of many liver diseases that lead to abnormal structural and functional degradation commonly caused by alcoholism, hepatitis B and C, and fatty liver disease. The disease causes cirrhosis which then damages and destroys cells and tissue inside the liver. After the damage, the inflammation and repair processes result in the formation of scar tissue. Then the remaining healthy liver cells attempt to replace the cells that have died, resulting in clusters of newly formed liver cells within the scar tissues.

In cirrhosis, the relationship between blood and liver cells is destroyed. Even though the liver cells that survive or are newly-formed may be able to produce and remove substances from the blood, they do not have the normal, intimate relationship with the blood, and this interferes with the liver cells' ability to add or remove substances from the blood. In addition, the scarring within the cirrhotic liver obstructs the flow of blood through the liver and to the liver cells. As a result of the obstruction to the flow of blood through the liver, blood "backs-up" in the portal vein, and the pressure in the portal vein increases, a condition called portal hypertension. Because of the obstruction to flow and high pressures in the portal vein, blood in the portal vein seeks other veins in which to return to the heart, veins with lower pressures that bypass the liver.

Unfortunately, the diseased liver is unable to add or remove substances from blood that bypass it. It is a combination of reduced numbers of liver cells, loss of the normal contact between blood passing through the liver and the liver cells, and blood bypassing the liver that leads to many of the manifestations of cirrhosis.

Cirrhotic patients may present with various sequelae of hepatic decompensation, including variceal hemorrhage, ascites, hepatic encephalopathy, and hepatic and renal failure.

(a) (b)
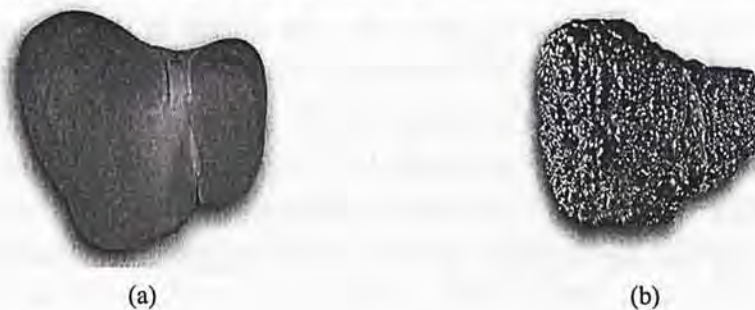
Figure 3.1: The pictures of both normal liver (a) and liver with cirrhosis (b) from humans (from http://www.indianetzone.com/1/cirrhosis_liver.htm).

3.1.3 The trend of liver cirrhosis
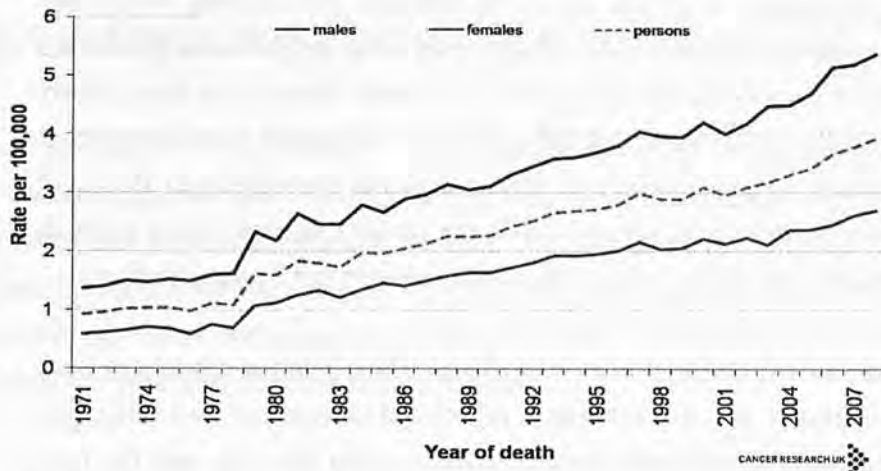
Figure 3.2: The age-standardized mortality rates from liver cirrhosis between 1971 and 2008 for the UK
(http://info.cancerresearchuk.org/cancerstats/types/liver/mortality/index.htm)

According to a liver cirrhosis report from Cancer Research UK in 2009,there is a higher mortality rate in males than in females and rates for both genders have increased over the last three decades from 1 per 100000 in 1971 to 4 per 100000 in 2008(shown Figure 3.2). Cirrhosis is also a risk factor for the development of Hepatocellular Carcinoma (HCC) which is the fifth most common cancer worldwide and its incidence is increasing and will likely continue for decades[50]. It is found that about 80% patients with HCC have cirrhosis [51]. The one year survival rate for patients diagnosed with HCC is very low.

Resection of HCC has become a safe operation with very low operative mortality as a result of advances in surgical techniques. However, the 1-year, 3-year and 5-year probabilities of HCC recurrence after resection were reported to be 19%, 54% and 70%, respectively [52]. Therefore early diagnosis of cirrhosis is needed to prevent HCC and thus improve survival rates. This is strong motivation to research potential diagnostic techniques. Known risk factors for recurrence include cirrhosis of the liver, chronic active hepatitis,

hepatitis C virus infection, high number of nodules affected, vascular invasion and disrupted tumor capsule.

Compared with non-cirrhotic cases, resections in cirrhotic livers can be technically more challenging. Of more concern is the problem of reliably estimating the functional capacity of a cirrhotic liver and its propensity to develop new malignant lesions [53]. An earlier paper has reported differences in dielectric parameters between the normal and cirrhotic areas in the microwave region [54]. This indicates that the formation of new structures in the liver during the cirrhosis process may lead to changes of the dielectric properties.

3.1.4 Technique for diagnosing liver cirrhosis

To date, the non-invasive diagnostic tests available from clinical practice are not sensitive or specific enough to detect occult liver injury at early or intermediate stages. Liver biopsy is the standard of reference for diagnosis and staging of liver cirrhosis. However, it is an invasive procedure with possible complications [55]. Histological assessment of fibrosis is also an inherently subjective process, and subject to sampling variability [56]. The extent of variations from observer interpretation by expert histopathologists may be as high as 20% [57]. These limitations make liver biopsy unsuitable for diagnosis and longitudinal monitoring in the general population.

To better manage individuals with progressive cirrhosis, especially those who would benefit from early intervention, a reproducible and reliable non-invasive method is needed to evaluate disease progression, to monitor responses to drug treatment, and to benefit epidemiologic research. Terahertz spectroscopy has already been demonstrated to be promising in characterizing different chemical components [58-60]. Apart from structural deformations, chemical changes in biological objects can also be caused by illnesses. If terahertz imaging can be effectively used to diagnose the liver cirrhosis, it would be of great benefit to clinicians.

3.2 Experiment protocol

3.2.1 Formalin fixing

Formalin-fixing is the most common preservation technique used on histologically prepared tissues. It would be useful to know if there have been more terahertz contrast if the samples had been measured in a fresh state, or conversely if the fixing process has enhanced the terahertz contrast. The purpose of this study is to determine and understand the ability of TPI to differentiate between healthy and cirrhotic rat liver tissue types in reflection geometry. In our previous work we have shown that formalin fixing of healthy tissue samples affects their terahertz properties and may reduce the image contrast between tissue types [61]. In this study, we use formalin to fix the samples, which will also cause some dehydration. This will help determine how much of the contrast between terahertz measurements of cirrhotic and healthy liver is due to changes in water content. To this end we calculate the frequency dependent refractive index and absorption coefficient of the samples and relate the results to water content and structural changes.

3.2.2 Sample preparation
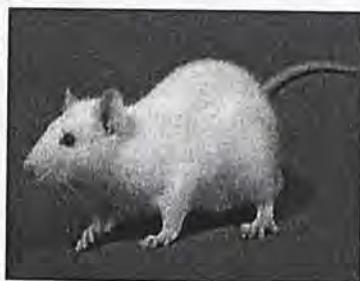
Figure 3.3: Four-week Male Sprague-Dawley rat

Laboratory rats share a high degree of homology with humans. In addition to their calmness and ease of handling, they can be inexpensively and easily maintained in laboratories. Therefore, they are commonly used for a variety of medical research purposes. In this chapter, all the tissue samples we used were

from laboratory rats. Four-week Male Sprague-Dawley rats with weight of 200-250g were used in this study (shown in Figure 3.3). The experimental protocol was approved by the institutional Animal Experiment Ethics Committee. The rats were bred at the Laboratory Animal Services Centre of the Department of Diagnostic Radiology and Organ Imaging. They were housed at 25°C under a 12-hour light, 12-hour dark cycle while receiving a standard commercial rat chow (Prolab RMH 2500, PMI Nutrition International LLC, Brentwood, USA) and water diet *ad libitum*.

Bile duct ligation (BDL) was performed under general anaesthesia. An upper abdominal incision was achieved using a sterile technique, and the common bile duct was isolated and double-ligated close to the liver, immediately below the bifurcation. The bile duct was severed between the two ligatures. Sham operation was performed on normal control rats in an identical manner, with the exception of ligation and transaction of the bile duct.

Four weeks post BDL or sham surgery, the rats were killed with an over-dose of pentobarbital, and the liver was harvested and studied *in vitro* within two hours of excision. Each liver specimen was cut into 6-8 pieces before measurement. This was carefully done so that the resulting pieces were flat and made good contact with the quartz window. To avoid later reflections after the quartz/sample, the typical slice thickness was several millimeters. The following photograph shows the normal (left) and cirrhotic (right) rat liver tissues samples.

Figure 3.4: Photograph of slices of normal(Left) and cirrhotic (Right) rat liver samples

3.2.3 Formalin fixing protocol
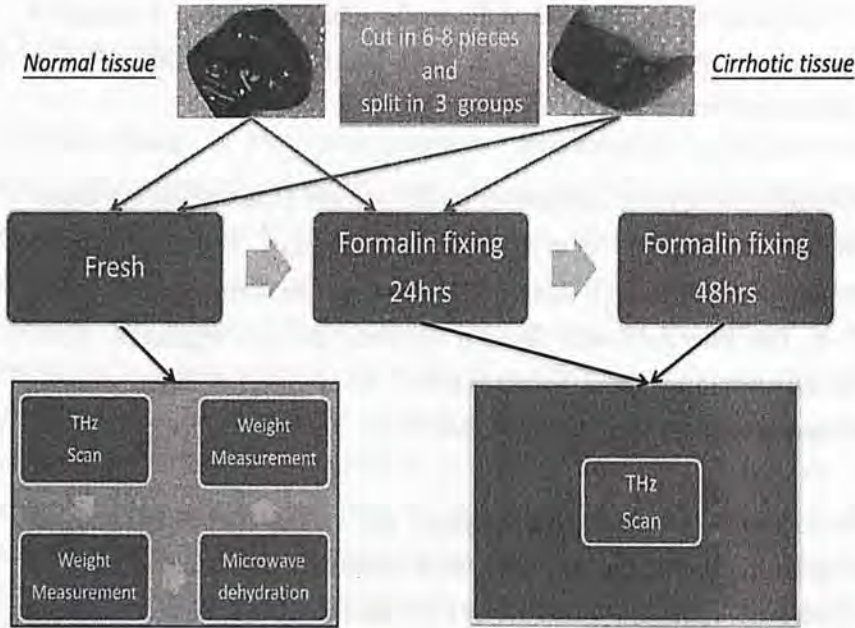
Figure 3.5: The overall picture of formalin fixing protocol and measurement processes.

After the fresh samples were imaged, aside from those samples used to determine water content, they were fixed in formalin and then imaged again after the fixing process had been completed. A standard protocol was followed for this process [62, 63] whereby non-buffered 10% formalin was used. The volume of formalin applied to the sample was at least 20 times the initial sample volume. The sample was then left to soak in the fixative in a sealed container and refrigerated at a constant temperature (4°C). Before measurement, the fixed tissue sample was washed under running water for 20 minutes to remove the excess formalin and then dried using blotting paper.

During imaging, since the fixed sample is rigid, gentle pressure was applied to the sample to ensure it made good contact with the quartz window. Each sample was measured after being fixed for 24 hours and 48 hours. No significant difference was observed between the 24hr and 48hr results and so we can assume that the fixing process was complete after 24hr. Only data

points where the sample had made good contact with the quartz window were used in the following results.

3.2.4 Histopathology

Additionally, following imaging, portions of the fresh specimens were fixed in 4% phosphate-buffered formaldehyde and embedded in paraffin. Sections of 5µm thick were de-waxed in xylene and rehydrated in a series of ethanol for standard Haematoxylin- and Eosin- (H&E) staining.

3.2.5 Protocol for measuring sample water content

A microwave oven was used to remove all the water from remaining fresh samples. A high performance electronic scale (OHAUS AR2140) was used to measure the weight of the samples before and after dehydration. The water content of the tissue samples was then calculated using **Eq 3.1**

$$\text{water content} = \frac{W_b - W_a}{W_b} * 100\%$$

Where W_b and W_a are the sample weights before and after dehydration.

(3.1)

3.3 Results and discussion

3.3.1 Optical parameters of the fresh and fixed samples

The terahertz properties of the healthy and cirrhotic rat samples measured in this study are illustrated in Figure 3.6.
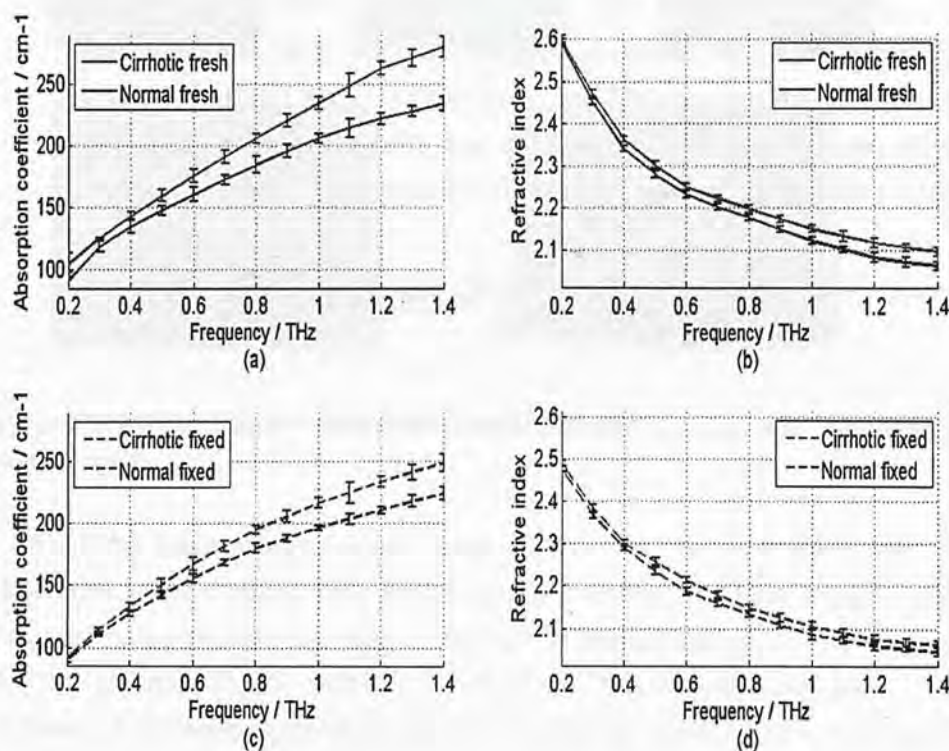
Figure 3.6: (a) Absorption coefficient of the fresh liver tissues, (b) Refractive index of the fresh liver tissues, (c) Absorption coefficient of the fixed liver tissues and (b) Refractive index of the fixed liver tissues. The error bars represent the 95% confidence intervals.

Both the fresh and the fixed samples the absorption coefficient and refractive index of the cirrhotic samples were higher than those of the normal samples. However the formalin fixing reduced the absolute values of the absorption coefficient and refractive index for both tissue types.

3.3.2 Consistency with previous results

In this study, the aim is to investigate differences between normal and cirrhotic tissue. One limitation of this study is that we were only able to obtain specimens from four rats. However, from our previous study of ten healthy rats [64] we have seen that the variation between rats of healthy liver tissue is small. In Figure 3.7 we plot the mean absorption coefficient from the ten rats used in our previous study alongside the mean absorption coefficient from the fresh tissue samples from the two healthy rats used in this study. The data agree within experimental error over the majority of the frequency range investigated. One reason for any slight discrepancies is variation in water content. The water contents of measured samples from the two healthy rats used in this study were 71% and 75%. Unfortunately the water content was not measured in our previous study for comparison.
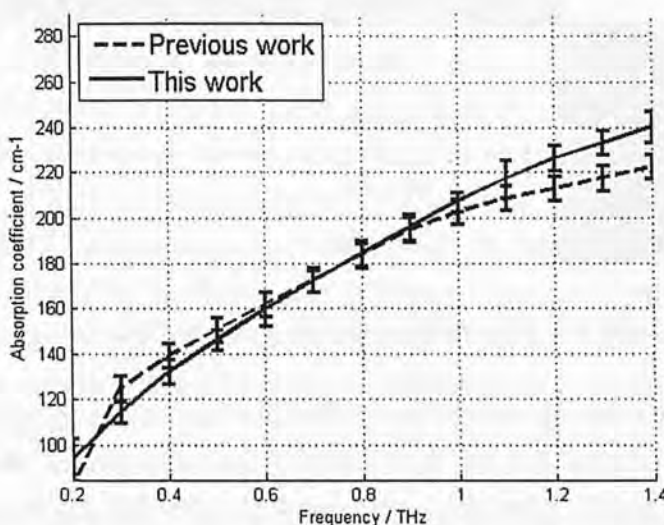
Figure 3.7: Absorption coefficient of freshly excised normal rat liver tissue measured in our previous work (black dashed line) and this work (blue line). The error bars represent 95% confidence intervals

3.3.3 The relationship between water content and optical parameters

The differences between the normal and cirrhotic samples are more prominent in the absorption coefficient than in the refractive index – the absorption coefficient of the fresh cirrhotic tissue is significantly higher than that of the fresh normal tissue across the majority of the frequency range measured. In previous studies in the microwave region it has been suggested that the higher absorption observed in diseased tissue is due to increased water content [65]. The water content of the rats ranged from 71% (healthy rat) to 83% (cirrhotic rat). The details are given in Table 3.1

	Type	Water Content/ %
Rat 1	Normal	71
Rat 2	Cirrhotic	81
Rat 3	Normal	75
Rat 4	Cirrhotic	83

Table 3.1: Percentage water content and rat type.

Figure 3.8 shows that the absorption coefficient of the tissues increases with increasing water content. For the three higher frequencies plotted, there is a pronounced non-linearity when the water content is above 80% as the samples with water content greater than 80% were cirrhotic. This graph therefore helps to illustrate the point that the presence of cirrhosis increases the absorption coefficient beyond what would be expected for simply increased water content. Namely, there are structural changes occurring which also increase the absorption coefficient of the tissue.
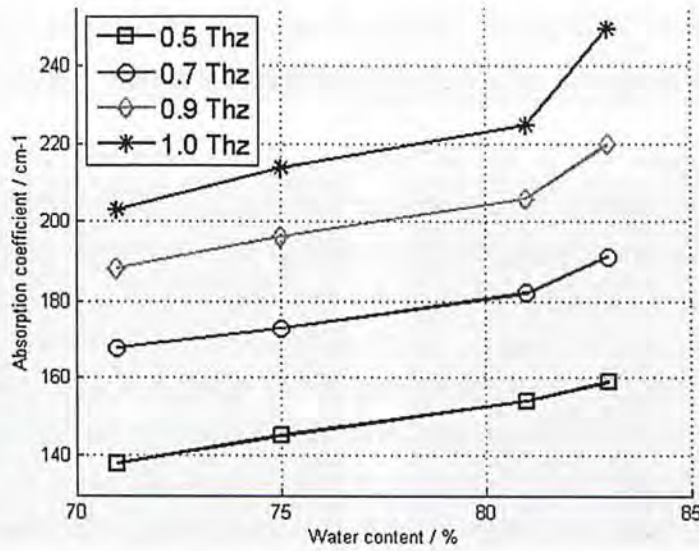
Figure3.8: A graph illustrating the absorption coefficient of the tissues increases with increasing water content. Data for 0.5-1THz are plotted

After fixing in formalin, the water contents of the samples decreased but their structures were preserved. Both the refractive index and absorption coefficient decreased due to the reduced water content. However, there is still a clear difference between the absorption coefficient of the fixed normal and cirrhotic samples. Since the water content of the tissues will have been significantly reduced by the fixing, this difference is primarily attributed to the differences in the tissue structure and composition. It is possible that some of the difference may be due to differences in remaining water content and we will estimate this below.

As illustrated in Figure 3.9, the difference between the cirrhotic and normal tissue absorption coefficients of the fresh samples is greater than that of the fixed samples and so we can deduce that the terahertz measurements of the fresh samples detected both changes in water content and structural changes. Area A predominantly represents the difference in absorption due to water and Area B predominantly represents the difference in absorption due to structural changes. We include the word "predominantly" in case there is any remaining water after fixation contributing to the difference or the formalin fixing caused any increase in the difference due to cross-linking bonds.

To obtain an upper limit on the amount of remaining water contributing to area B, we consider the absorption coefficient difference at 0.2THz and assume that it is purely due to a difference in water content. At this frequency, there is $2.8cm^{-1}$ contributed by area B. From terahertz spectroscopy of water [66] the absorption coefficient of water at 0.2 THz is $109cm^{-1}$. Thus 2.6% (2.8/109*100%) is the maximum percentage of the absorption coefficient of water contributing to the difference at 0.2THz, and all other frequencies, and so we plot 2.6% of the absorption coefficient of water across the frequency range in Figure 3.9 to give an upper estimate of the amount of area B that could be due to remaining water.
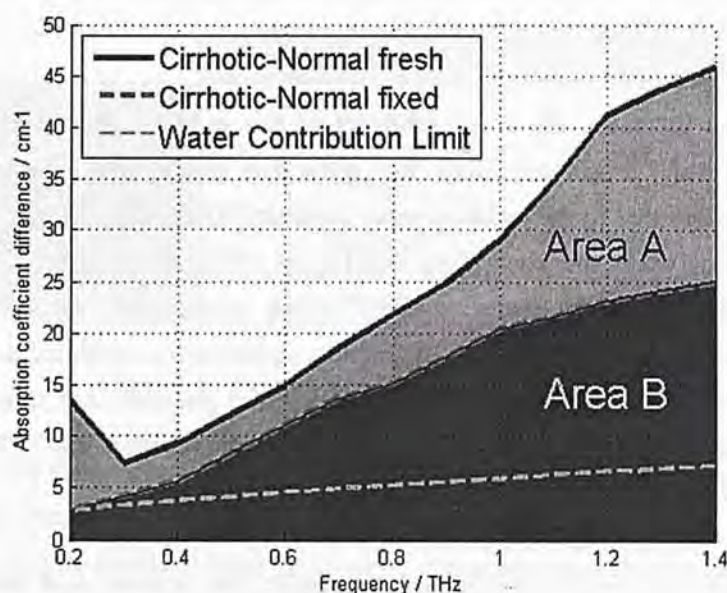
Figure 3.9: The solid blue line traces the absorption coefficient of the fresh cirrotic minus that of the fresh healthy tissue and the dashed pink line traces the difference for the fixed samples. Therefore Area A predominantly represents the difference in absorption due to water and Area B predominantly represents the difference in absorption due to structural changes. The dashed green line gives an upper limit of the contribution to Area B that could be due to remaining water.

To determine the structural changes that occurred, we examine the histopathology results in Figure 3.10. The control rat liver results show normal liver structure, while the BDL rat results demonstrated evidence of biliary

cirrhosis and nodular liver with intense ductular proliferation, fibrotic bridges and more pronounced inflammatory infiltration.
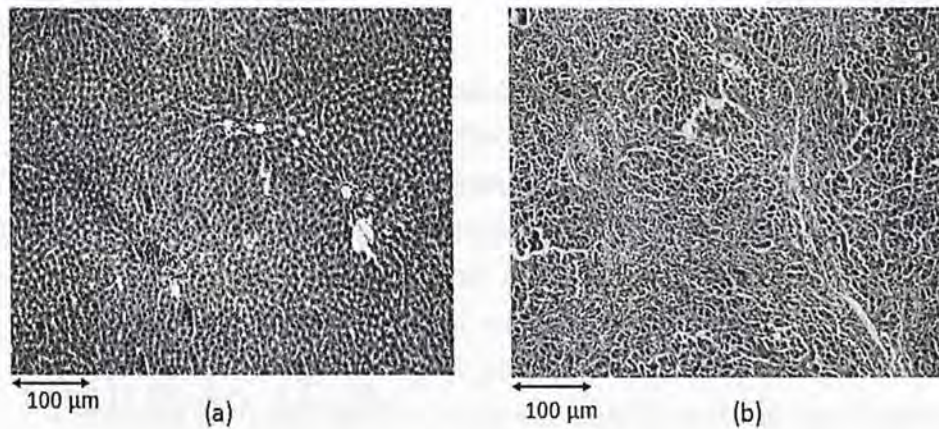
Figure 3.10:Microscopy pictures of Haematoxylin- and Eosin stained samples from (a) control rat liver and (b) rat four weeks post biliary duct ligation.

From Figure 3.9 we see that for frequencies above 0.4 THz, structural changes contribute to 50-66% of the total change in absorption coefficient and thus water is not the sole, nor even the dominant source of contrast in the terahertz properties of liver cirrhosis. This is a very significant result as previously it has been thought that water was the main source of contrast. In this study, for the first time, we have quantitatively shown that this is not the case, thus providing strong motivation for further research into probing macroscopic structures with terahertz light.

3.3.4 Conclusion

In this study, we have measured the terahertz properties of freshly harvested healthy and cirrhotic rat liver samples in reflection geometry with a hand-held terahertz probe. We found that the absorption coefficient of the cirrhotic tissue is significantly higher than that of the healthy tissue. Furthermore, we found that the difference is still significant after formalin fixing and this tells us that the difference is not only due to changes in water content, but also due to structural changes. Thus terahertz imaging is able to detect both changes in water content and structural changes that occur in tissue due to the presence of cirrhosis.

Chapter 4 In-*vivo* experiment: imaging of human skin

Previous TPI of breast cancer [67],skin cancer[41]and dental caries[44] are the good examples to illustrate the feasibility of TPI in medical applications. Based on the study of skin from Pickwell *et al*, in this thesis we further investigate the *in vivo* time domain terahertz response of human skin with different positions under different temperature and humidity.

4.1 Human skin

4.1.1 The structure of human skin
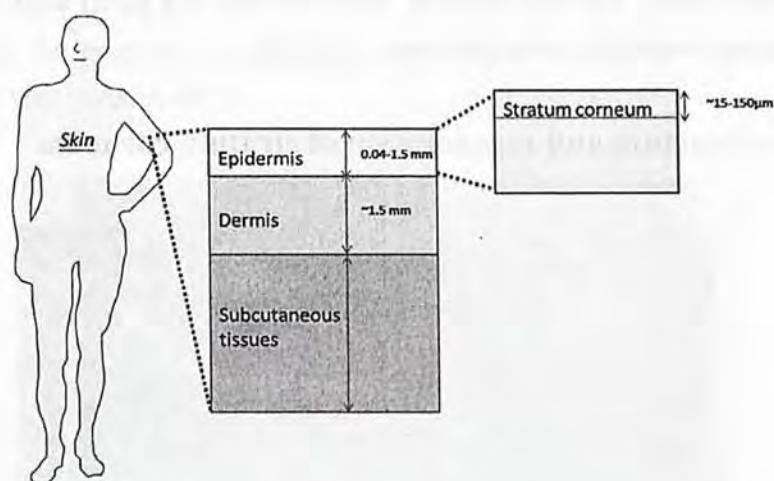
Figure 4.1: Three layers of human skin: the epidermis, dermis and subcutaneous tissues. The stratum corneum lies above the epidermis.

For humans, normally we can divide the skin into three layers which are epidermis (top layer), dermis (middle layer) and the subcutaneous tissues (shown schematically in Figure 4.1). The outermost layer of the epidermis is the stratum corneum (also called the horny layer), this layer is exposed and so is often drier than the tissue beneath it.

4.1.2 Skin thickness

The whole epidermis is only 0.04-1.5mm thick while the stratum corneum (SC) is just about 15-150 µm thick[68], depending on location. For instance on the palm of the hand or soles of the feet it is around 150 µm whereas on the volar forearm it is closer to 15 µm. Skin thickness is also affected by the amount of pressure or friction it has been subjected to[68]. In previous studies, terahertz responses for different areas of skin (namely the volar forearm, dorsal forearm and palm) were studied both on flat-bed and hand-held probe TPI systems[66, 69].

4.1.3 The structure and regeneration of stratum corneum
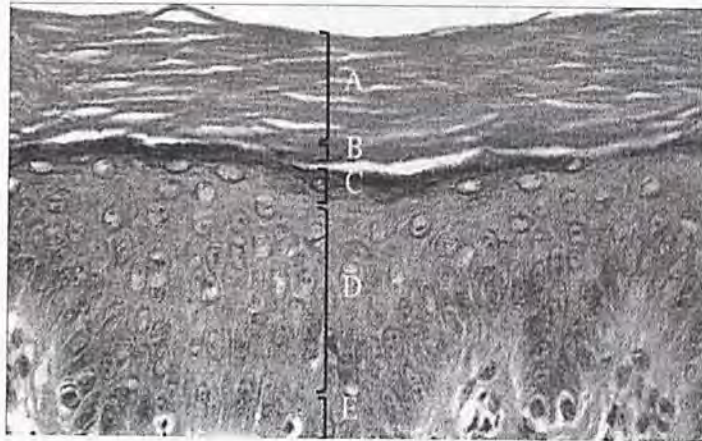
Figure 4.2: The structure of epidermis: A.Stratum corneum, B.Stratum lucidum, C.Stratum granulosum, D.Prickle cell layer, E.Basal cell layer[70]

Generally we can divide the epidermis into 5 layers: A. Stratum corneum (cornfield layer), B. Stratum lucidum (clear/translucent layer), C. Stratum granulosum (granular layer), D. Prickle cell layer (spinous layer), and E. Basal cell layer (basal/germinal layer). (Figure 4.2) The epidermis acts as the body's major barrier against an inhospitable environment.

The formation of the epidermis begins in the cells covering the embryo after neurulationof the central nervous system.This begins with a temporary outer layer, the periderm, which is disposed of once the inner basal layer or stratum germinativumis formed. This inner layer is a germinal epithelium that gives rise to all epidermal cells. It divides to form the stratum spinosum. The cells of these two layers, together called the Malpighian layer(s) after Marcello Malpighi, divide to form the stratum granulosum of the epidermis. The cells in the granular layer do not divide, but instead form skin cells called keratinocytes from the granules of keratin. These skin cells finally migrate to form stratum corneum, the outermost epidermal layer, where the cells become flattened sacks with their nuclei located at one end of the cell.

To model the epidermis regeneration after irritant dermatitis, the tape stripping experiment was introduced[71].
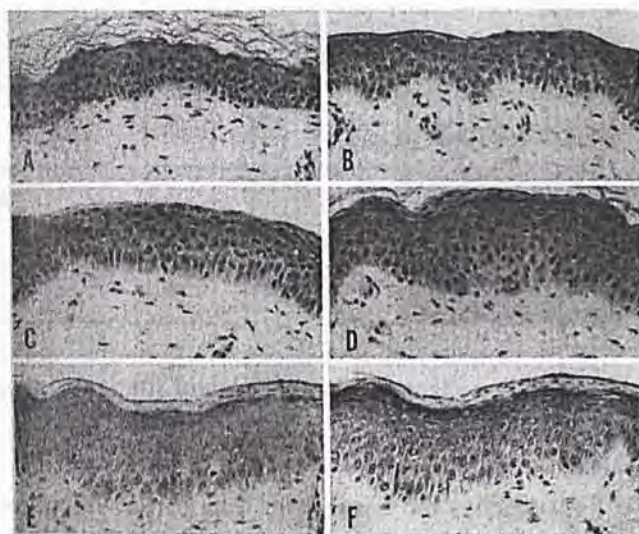
Figure 4.3: Epidermal response to tape stripping A. Control, B. After 12 hrs, C. After 24 hrs, D. After 36 hr, E.Aftre 40hrs and F.After 48 hrs[71]

Figure 4.3 shows the regenerative sequence of the epidermal response to tape stripping within 48 hrs. After removing the horny layer by tape stripping, the prickle cells start to dehydrate. In this case edema and exudates remain minimal. One half hour after stripping, the uppermost cells look parakeratotic as they begin to dry out. Most of the prickle cells eventually are involved in this process, while the basal cells become very large. Their clear appearance is due to accumulation of glycogen. After 36 to 48 hr, a great burst of mitotic activity develops in the basal layer and replaces within a few days the cells lost through stripping and dehydration. A new and usually hyperplasic granular layer is formed, followed by maturation of a new horny layer. Most of the original epidermis is exfoliated as a parakeratotic scale.

4.1.4 Stratum corneum related Skin disease

Abnormal change of the thickness of stratum corneum (i.e sudden changes to too thin or too thick) also can reveal symptoms of some skin diseases, for example, hyperkeratosis and eczema[68]. Table 4.1 shows the corresponding change of the thickness of stratum corneum due to different skin diseases.

Disease	The change of stratum corneum
Hyperkeratosis	Thicker
Eczema	Thicker
Epidermal atrophy	Thinner

Table 4.1: The corresponding change of the thickness of stratum corneum due to different skin diseases.

If too much UV light reaches the basal layer then it may damage the DNA. These cells will appear as a tumor, known as basal cell carcinoma, which is normally confined within the stratum corneum, though they may also invade the upper layer of the dermis. However, if a melanocyte is damaged then the arising tumor, known as melanoma, can spread into the dermis and is also able to corrupt the blood vessels. In this way the cancer may enter the blood stream and metastasize to secondary sites.

Therefore if we can understand and trace the change of the thickness of the stratum corneum by non-invasive terahertz measurements, it really can help to diagnosis a lot of skin diseases earlier which can prevent the situation from deteriorating.

4.2 Combing reflections of electromagnetic wave

For the sake of the readability to reader, before we step into the experiment section, a brief review to "combining reflections" of electromagnetic wave would be given.

As was mentioned in Chapter 2, once an electromagnetic wave crosses from a material to another material with a different refractive index, besides the refraction, reflection would also occur. Based on the difference between the refractive index of two materials, it may induce a π (180°) phase change to the reflection pulse. The following graphs are showing the actual situation. When the wave is reflected by a medium of higher refractive index (Case1: n1<n2) there is a π (180°) phase change otherwise there is no phase change. Figure 4.5shows the process of combining reflections resulted by reflection of a wave from a 2 layer material.

Case1: n₁<n₂   **Case2: n₁>n₂**
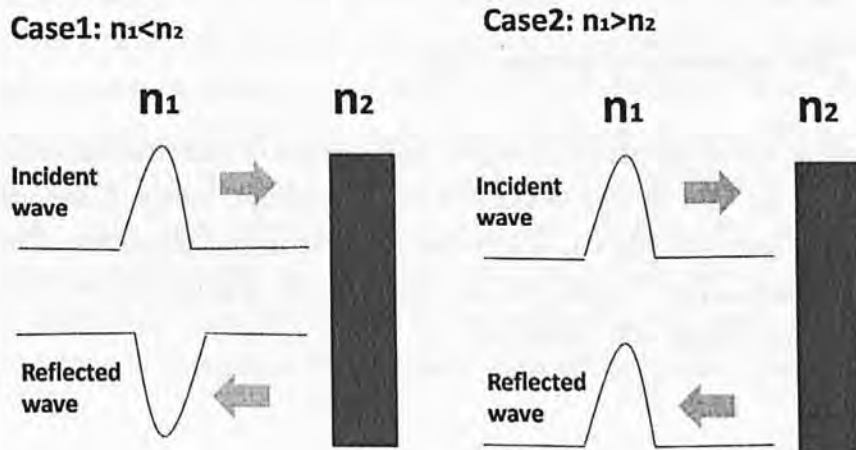
Figure.4.4: Two different type of reflections according to the difference between two mediums.
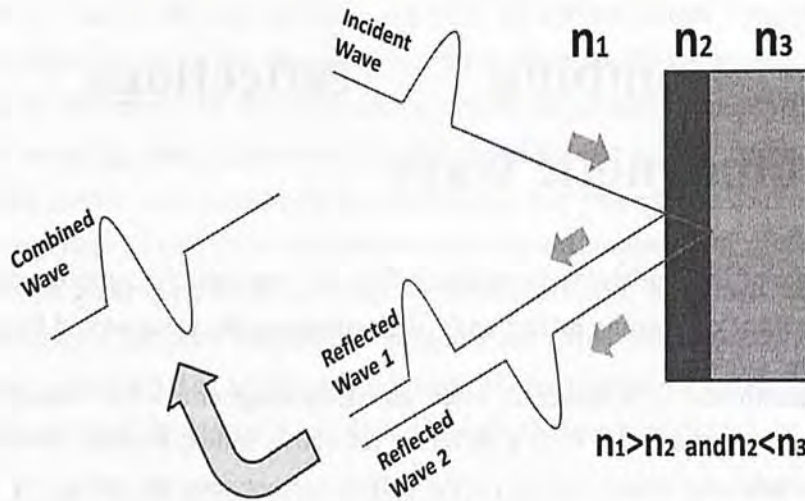
Figure.4.5: The process of combing reflections resulted by emitting a wave on to a 2 layer material.

4.3 Experiment protocol

4.3.1 THz response of human skin

According to our experience through a large number of measurement results, we can classify all the skin surface reflections into two groups. Group A and group B are shown in Figure.4.6. Mainly, this is due to the changing properties of the stratum corneum, such as the thickness and the water content. It is these kinds of change that will result the change of RI of the SC.
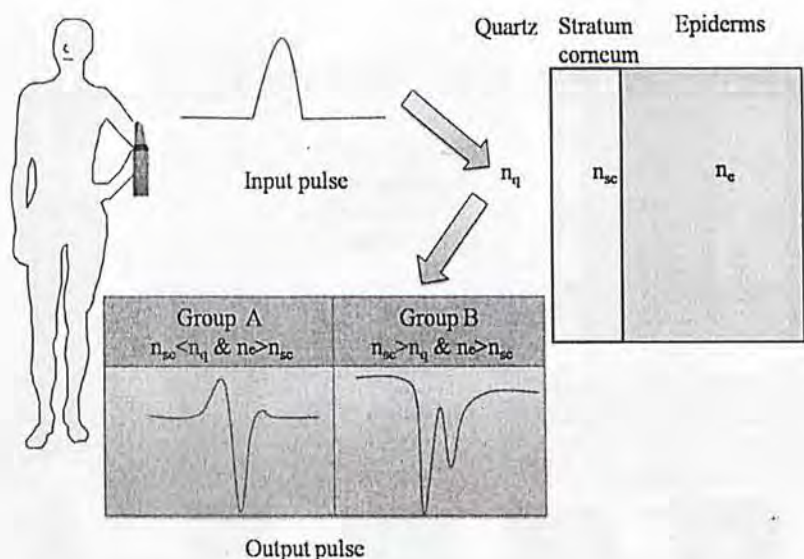
Figure.4.6: Two different groups of skin reflections Group A (when the refractive index of stratum corneum is smaller than that in quartz), Group B (when the refractive index of stratum corneum is bigger than that in quartz)

4.3.2 Protocol for measuring human skin

Ten subjects, aged between 24 and 29 years, were invited to join the investigation. Among the volunteers, 7 are male and 3 are female. The whole experiment was conducted over5 days with different temperature and humidity. Five different skin surface measurements on the face, arm and hand were included in this study. They are the centre of the forehead (Position A), the centre of the cheek (Position B), the centre of the chin (Position C), the centre of the right dorsal forearm (Position D) and the centre of the right palm (Position E). Photographs showing the measurement positioning are given in Figure 4.7. In order to maintain a clean surface of the probe after every measurement, the surface was cleaned with alcohol to make sure that no oil/grease/moisture from any skin measurement would affect the next measurement.
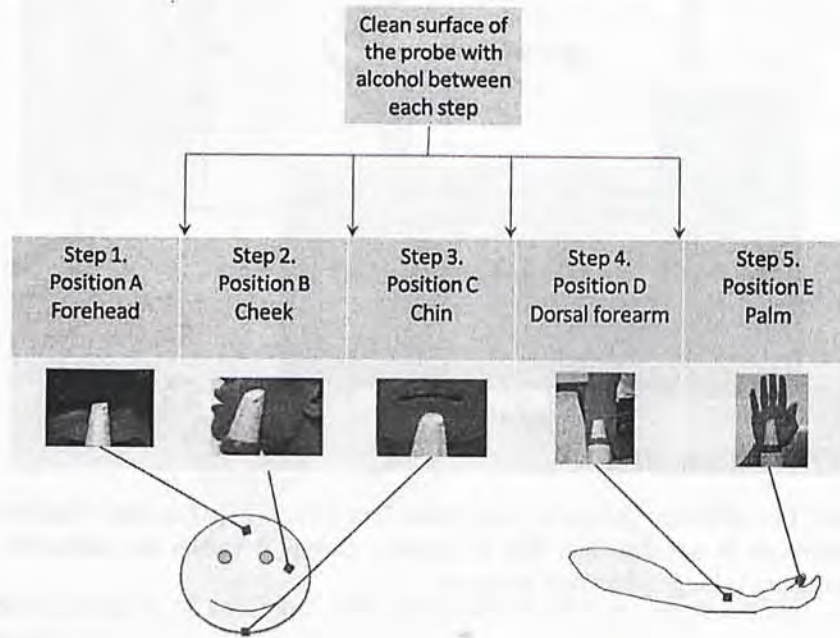
Figure 4.7: The experiment protocol with five different skin surfaces (Forhead, Cheek, Chin, Dorsal forearm and Palm).

4.4 Results and discussion

4.4.1 The variation due to the position

Figure. 4.7 shows all the average impulse waveforms from the five target locations to those ten subjects in five different days after they were processed using DGF (See Chapter 2).Typically, in every waveform there is a peak followed by a trough. The amplitude of the initial peak is dependent on the properties of the skin such as surface dryness and so we see the variation in this amplitude between measurement sites.
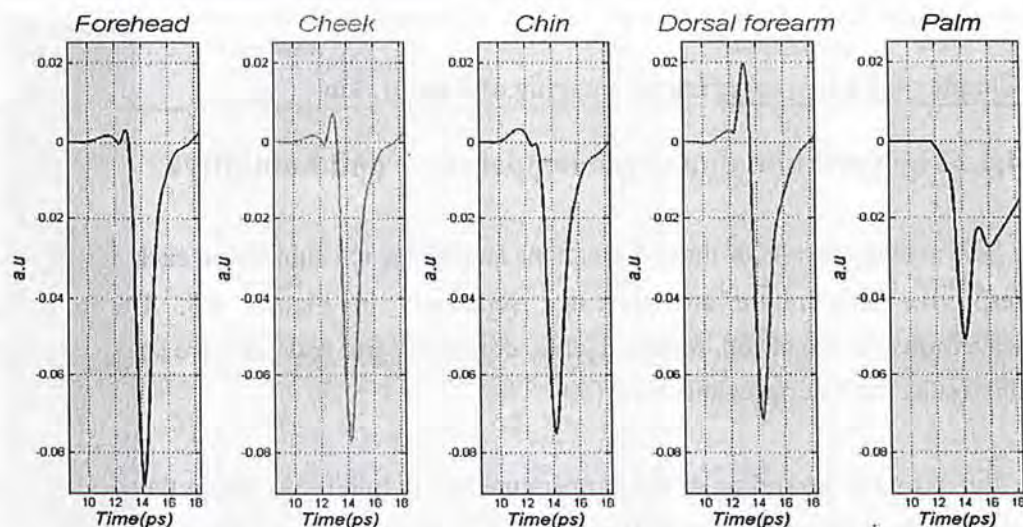
Figure. 4.7: The average impulse waveforms from the five target locations to those ten subjects in five different days measurement.

Table 4.2 shows the respective maximum and minimum amplitudes for the five different measuring places to subjects. From the table, the maximum amplitude of the dorsal forearm is the highest – this is due to the hair on the dorsal forearm creating an air gap which allows a positive peak to propagate until it reaches the skin, at which point it is inverted. The other areas of skin measured were not hairy and have similar (lower) peak values. Since the SC on the palm is thick enough to be resolved by TPI, there are two troughs in the reflected waveform. However in the other skin areas measured, the SC could not be resolved and only one reflected trough was observed.

Location	Maximum amplitude (a.u)	Minimum amplitude (a.u)
Forehead	0.003	-0.088
Cheek	0.007	-0.077
Chin	0.003	-0.075
Dorsal forearm	0.019	-0.071
Palm	0.000	-0.050

Table 4.2: The maximum and minimum amplitudes of each average waveform to five different measuring places among ten subjects in five different days.

4.4.2The variation due to the temperature and humidity

The average results of those 5 positions among the ten subjects in each day and the respective temperature are presented separately in Figure. 4.8. The resulting waveforms for the cheek, forehead, chin, dorsal forearm and palm are consistent with the results from our previous study[33].

Furthermore, according to the temperature and humidity we group the five days of data into two groups: the cold (Blue color, 8,22 Feb) and the warm group (Red color, 19 Jun, 15 Mar, 11April). As can be seen, there is a big difference between the result of the cold and hot group. Clearly, the peak to peak value of the resulting waveform in the cold group has relative smaller amplitude for all five different skin positions which may be caused by the difference in temperature and humidity (See Figure 4.9).
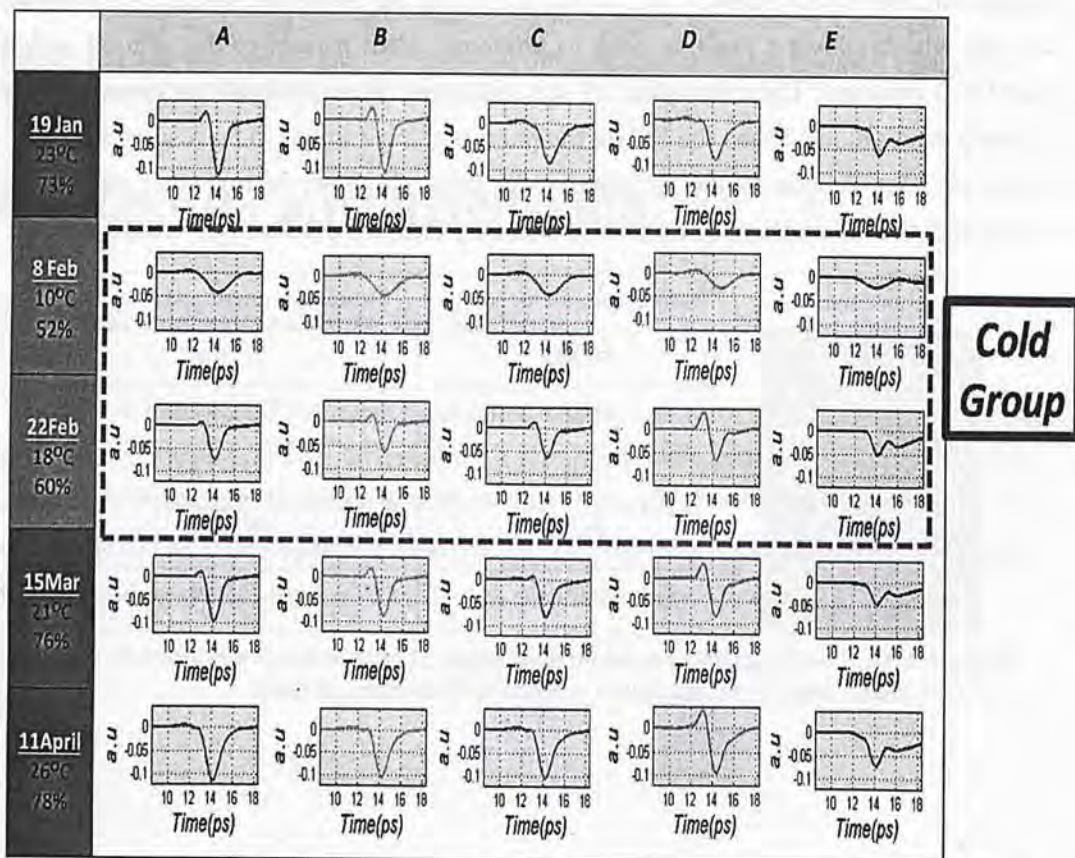
Figure. 4.8: Measuing result for five days with different temperature on five differernt skin areas.
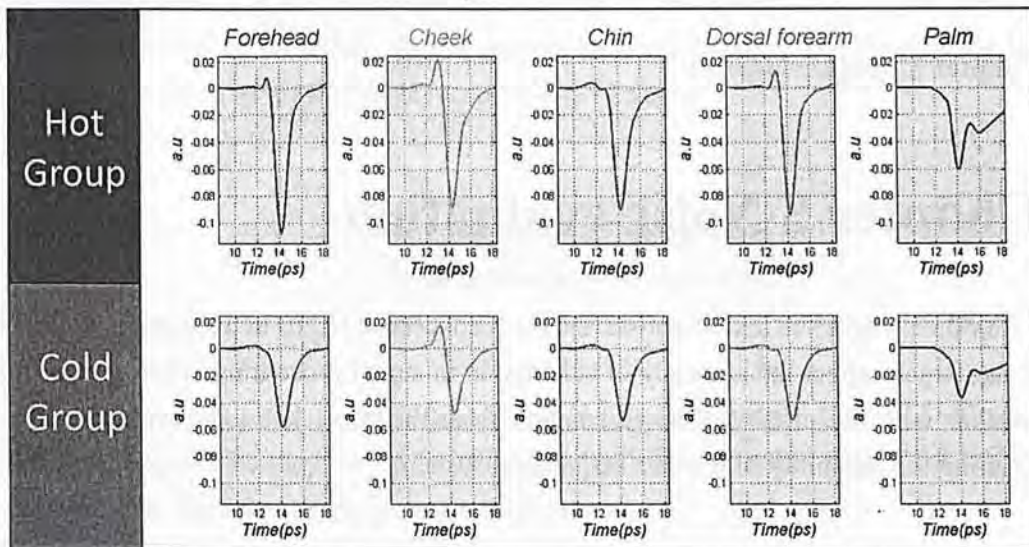
Figure. 4.9: The comparsion between the "Hot group" and "Cold Group" on the five different mearsuing skin areas.

4.4.3 Discussion

In this study the THz probe attachment was used to measure the skin on five different locations namely the centre of the forehead, the centre of the cheek, the centre of the chin, the centre of the right dorsal forearm and the centre of the right palm. We found that the resulting waveforms from the dorsal forearm and palm measured on the warm days using the new THz probe were consistent with previous work by Pickwell *et al* using the flatbed imaging system [6]. The cold weather affected the skin properties such that the resulting waveforms were reduced in amplitude.

These results show that TPI is very sensitive to skin properties therefore has the potential for monitoring skin disease and repair. And characterizing different skin areas is important because if TPI is to be used to diagnose skin cancer in the future, the THz properties of healthy skin must be well understood first. By doing this, we can form a step towards developing improved imaging algorithms for diagnostic detection of skin diseases and skin cancer.

Chapter 5 Noise evaluation

For most engineers and scientists, the most concerned factor in a system is noise as it can largely affect the accuracy of calculation in signal processing. Therefore being familiar with the effect on the calculation from the noise is an important step for ensuring the reliability of the data acquisition system.

5.1 The main noise source

For our TPI, the main sources of noise comes from fluctuations in the ultrafast femtosecond laser, Johnson noise and shot noise [72-75], and all of them can be treated as stationary Gaussian processes. Due to the relative poor power efficiency of photoconductive antennas, the output power in a typical pulsed system employing photoconductor is low. Although highly sensitive detectors can be used to suppress the background noise, sometimes the data analysis is still very difficult due to a bad SNR, especially when probing objects that strongly absorb THz radiation, for instance biological tissues. To accurately characterize a sample, good quality signals with high SNR are desired [76, 77].

5.2 SNR and DR

5.2.1 Signal to noise ratio (SNR)

There are a number of ways to define SNR which is also a common criterion to evaluate the system performance. One common method to define SNR is the ratio between the mean magnitude of the signal and the noise respectively (**Eq 5.1**).

$$SNR = \frac{\text{mean magnitude of the signal}}{\text{mean magnitude of the noise}}$$

(Eq 5.1)

Actually, both the signal and noise can be defined in several ways, for example in

the time domain or in the frequency domain [78]. In our system, we choose multiple datasets to estimate the SNR. Signal and noise are calculated from mean and the standard deviation of these datasets respectively **(Eq 5.2)**.

$$SNR(\omega) = \frac{\text{mean magnitude of the datasset } (\omega)}{\text{SD magnitude of the dataset} (\omega)}$$

(Eq 5.2)

In addition, since the signal is broadband in a pulsed system, the SNR values at different frequencies may vary a lot (Figure 5.1(a)). The signal in Figure 5.1 (a) was calculated by **Eq 5.2** with measuring a gold mirror.

5.2.2 Dynamic range (DR)

Besides SNR, another comparable indicator is the system dynamic range (DR). DR at a particular frequency in a pulsed system can be defined as the spectral amplitude in this frequency over the root mean square (RMS) of the noise floor **(Eq 5.3)**.

$$DR(\omega) = \frac{\text{Spectral magnitude } (\omega)}{\text{RMS of noise floor}}$$

(Eq 5.3)

DR in a pulsed system is also dependent on frequency. Sometimes the maximum DR is simply quoted as the system DR. Figure 5.1(b) shows the dynamic range distribution over frequency. The spectral data was from a single point measurement and noise floor was estimated by the RMS of spectra greater than 3.5 THz. The spectra in this figure have been normalized to the noise floor (estimated as 61.9) with a maximal DR of 2512 around 0.21 THz. Similarly to SNR the data in Figure 5.1(b) is measuring with a gold mirror.
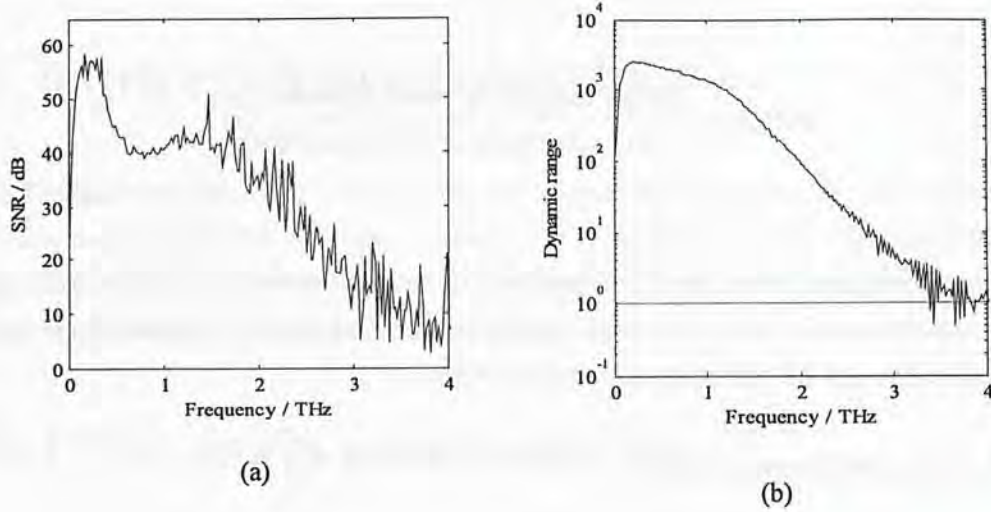
Figure. 5.1: SNR (a) and DR (b) distribution from 0 THz to 4 THz

5.2.3 SNR VS DR

For DR, only a single dataset was used but for evaluating SNR, multiple datasets were obtained by repeatedly measuring the central point of the image window. Regarding Figure 5.1(both (a) and (b)),it can be seen that both SNR and DR decline gradually in the high frequency band. Compared with DR which changes gently above the noise floor, SNR has shown greater fluctuations.

Although there is no direct relationship between the values of SNR and DR [78], the maximum values of SNR and DR appear in the same area, in our case around 0.2 THz. It is worth noting that at frequencies below 2 THz, the SNR can be as high as around 40 dB and is good for signal processing, whereas at higher frequencies, the SNR is deteriorating and becomes unsatisfactory. The reason why we chose the gold mirror to get the SNR and DR of the system is that mirror is highly reflective to THz radiation; the reflected light would have a very small loss compared to the incidence. As we are aiming to investigate very absorbing biological tissues, naturally the SNR of the detected waves from those water rich tissues will be worse than that from the mirror. As a result, the effective frequency band would be even narrower.

5.3 Simulation of noise impact on the complex refractive index

In this section, we are going to simulate and determine how the SNR and DR affect the both the RI and AC extracted from the measuring data from our hand-held probe TPI system.

5.3.1 Methodology

The first step in this simulation involves having to acquire the data from the air (reference) and gold mirror (incident) (see Figure 5.2) as we want to use them as a reference to make sure our model incident pulse and air reflection pulse are close to the actual data.
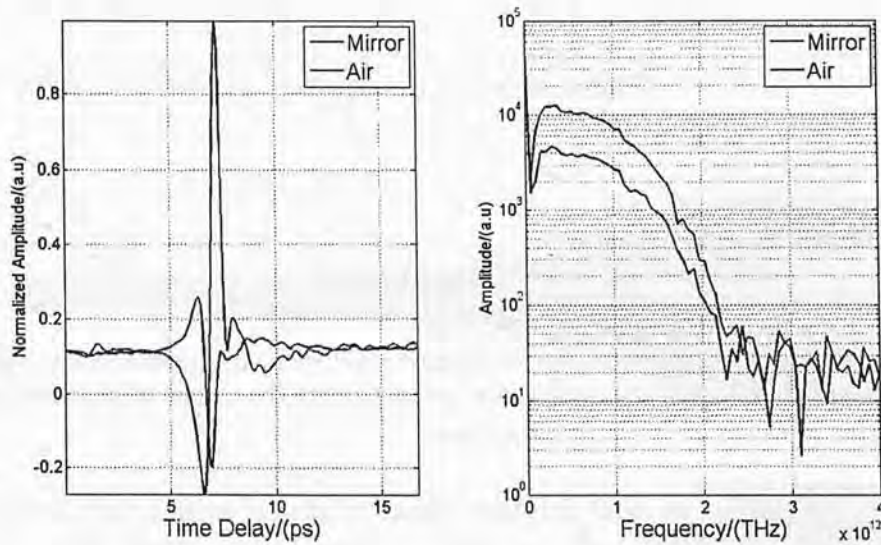
Figure 5.2: The actual data measuring from a gold mirror (Blue solid line) and air (Dark solid line) both in time domain(Left) and frequecny domain (Right).

We use a Double Gaussian function to model the incident pulse. By doing this the pulse using in the simulation can have similar power distributions over the frequency axis with the actual data. After getting the model simulating pulse, by using Fresnel's

equation and assuming the optical parameters of air and sample we can get both ideal simulated air and sample pulses. We assume the refractive index of air is 1 (sample is 2) and the absorption coefficient of air is 0 (sample is 100). The simulating result is shown in Figure 5.3. Regarding the both simulated incident and air pulse, we can see their spectra match the actual spectra very well below 2 THz, which was of our interest in this simulation work.
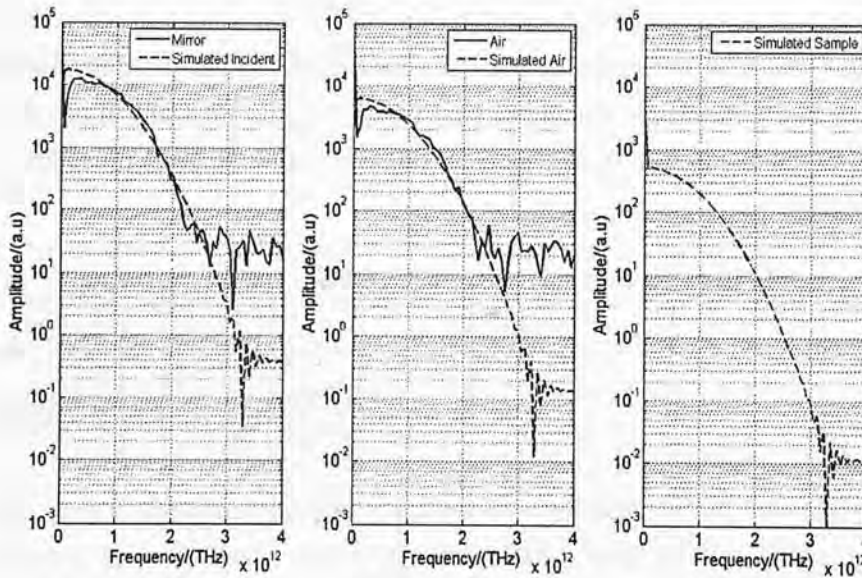
Figure. 5.3: (Left) The spectra of mirror reflection and simulated incident pulse, (Middle) The spectra of air reflection and simulated air pulse, (Right) The spectra of simulated sample pulse

After the preparation of ideal simulated pulses of air and sample, then we have to contaminate the signal according to different SNR (25dB, 35dB, 45dB, 55dB). Gaussian white noise was added to both the air and sample signals. The power of the noise was determined by the sample power (RMS) and a set value of SNR. Here the SNR was defined in the time domain as the power ratio between the signal (reference or sample) and the Gaussian noise (Figure 5.4). Then these contaminated signals were used to calculate the complex refractive index of the sample. At each noise level, the same step was repeated 500 times.
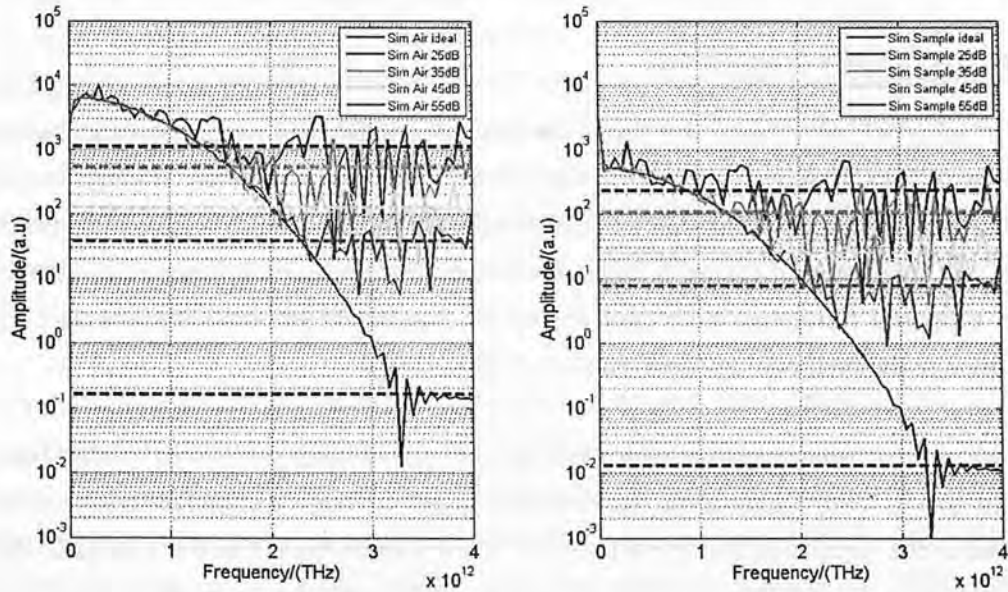
Figure. 5.4: The spectra of contaminated air(a) and sample(b) with different SNR (25 dB, 35 dB, 45 dB, 55 dB)

5.3.2 SNR: Simulation results and discussions
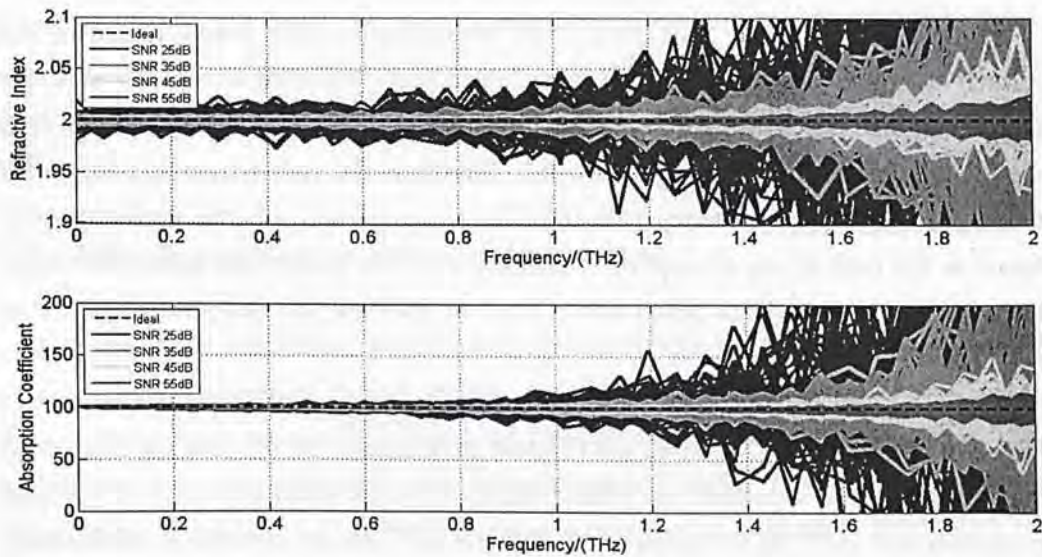
Figure. 5.5: The spectra of simulated result of refractive index (upper) and absorption coefficient contaminated air (lower) with different SNR (25 dB, 35 dB, 45 dB, 55 dB).

In this part, we present the simulated refractive index and absorption coefficient below 2 THz. Based on the SNR value of the signal, the results are divided into 4 groups, namely 25dB (Blue line), 35dB (Green line), 45dB (Yellow line), 55dB (Pink line), as illustrated in Figure 5.5.Thedark dashed lines inside the Figure 5.5 indicate the supposed refractive index and absorption coefficient of the sample which we defined in the methodology section. ($\mathbf{n} = 2, \mathbf{\alpha} = 100$).

We started from investigating a worst case of signal quality: SNR of 25 dB (Blue solid lines). With Regards to the refractive index, a huge difference can be seen between the simulation and the set values (Black dashed lines).Once we increase the frequency to higher than 0.6THz, the signal fluctuations increase even more. This indicates it would be almost impossible to extract **n** when the signal quality is so bad. However we can see that there is a quite acceptable performance existing in the case of absorption coefficient as long as the frequency is lower 0.8 THz. Similarly to refractive index we can see a serious deterioration after we increase the frequency higher than 1 THz which means we can only extract αwell during low frequency.

Next we move to the SNR with 35dB level (Green solid lines).Regarding the refractive index, clearly the performance is largely improved compared with the aforementioned case. But, still, once we increase the frequency higher than 0.7 THz, the fluctuation is deteriorating gradually. Therefore we can extract the refractive index just below the frequency with 0.7 THz. As expected, a better performance is found in the case of the absorption coefficient than the case of the refractive index. Here we can see a serious deterioration after we increase the frequency higher than 1.2 THz.

Now we increase the SNR to 45 dB (Yellow solid lines). We see that the simulation matches quite well with their set values, except for some small deviations in the high frequency end (1.2THz for refractive index and 1.4 THz for absorption coefficient). This indicates that in this case the results can be resolved with a good accuracy.

Finally the SNR was set to 55 dB (Purple solid lines), regarding to refractive index the simulation lines below 1.4 THz (1.6THz for absorption coefficient) are almost the same as the set lines.

When we extract the complex refractive index of an object, we are particularly interested in their profiles in the frequency domain. For different frequency components, since the individual power is different, the SNR at each frequency would be different. From the spectrum of Figure 5.5, it is clear that the SNR value is decreasing as the frequency increases. Consistently, for all 4 different SNR values, we can see a better performance in absorption coefficient than that in refractive index. The purpose of this simulation work is to get a rough idea on how the noise would affect the calculation accuracy.

In the simulation, since the signal and noise can be generated separately, it is easy to get the SNR of a single signal through the power ratio of the signal and the noise. However, in practice a detected waveform would inevitably be contaminated by the noise and they can hardly be separated. In other words, it is impossible to recover the real signal without any noise. This is why we typically estimate the SNR from multiple trials of detection. It should also be noted that to make the protocol simple, the level of noise added to the reference and sample signals was exactly the same. However, in practice they may be different due to the difference between the air and sample. In this sense, the SNR values we discussed in the simulation may not be the same as in the case of practical estimation. But we did see from the simulation that when the noise level was increased, the accuracy for the both refractive index and absorption coefficient would become problematic. More importantly, refractive index and absorption coefficient were similarly affected by the noise. And clearly the absorption coefficient appears to be affected slightly less severely than the refractive index

5.3.3 DR: Simulation results and discussions

With the above simulation, we qualitatively looked into the general impact of noise on the optical parameters. In this section, we aim to make a quantitative analysis of the accuracy of the results. To this end, we improved the simulation protocols and the sample spectrum was modeled with uniform power density. When white noise was added to the sample, since the white noise power was also uniformly distributed, the resulted SNR at all frequency components would be very close to a constant value.

Then this value is actually the DR as was defined at the beginning of this chapter. So in this way DR could be related to the accuracy of the results. The sample was the same as we defined in the last section (SNR simulation). Once the sample spectrum was determined, the reference spectrum can be derived. Then the remaining steps were repeated as in the previous simulation and the refractive index and absorption coefficient could be extracted. Similarly to the simulation with SNR, we simulated refractive index and absorption coefficient below 2 THz. Based on the DR value of the signal, the results are divided into 4 groups, namely 25dB, 35dB, 45dB, 55dB.After the simulation, we can find the difference in absorption coefficient αincreases as frequency increases. This means that when DR is the same, the calculated absorption coefficient at a lower frequency is more accurate than that at a higher frequency. Regarding to refractive index **n**, the higher DR, the more accurate refractive index **n** we can get. We define the maximum percentage difference (MPD) as the ratio between the maximum absolute difference (MAD) and the real value. Then we can use MPD values to represent the system accuracy. When DR was 25 dB, MPD values for n and α were calculated to be 6.1% and 0.5%, respectively. By changing DR to different values, MPD values at different noise levels could be found, as shown in Table 5.1.

DR	25 dB	35 dB	45 dB	55 dB
MPD (%)α	6.1	1.3	0.5	0.45
MPD(%)n	0.5	0.2	0.1	0.08

Table 5.1: MPD values at different noise level and DR

We further plot the above values in Figure 5.6 to show the relationship between MPD and DR. For a sample signal with a particular DR, the corresponding accuracy can be roughly estimated from this relationship, for example, when DR is 35 dB, the accuracy in terms of MPD is about 0.2% for n (or 1.3% for α). Similarly, when a given accuracy is allowed, the required DR can also be calculated.
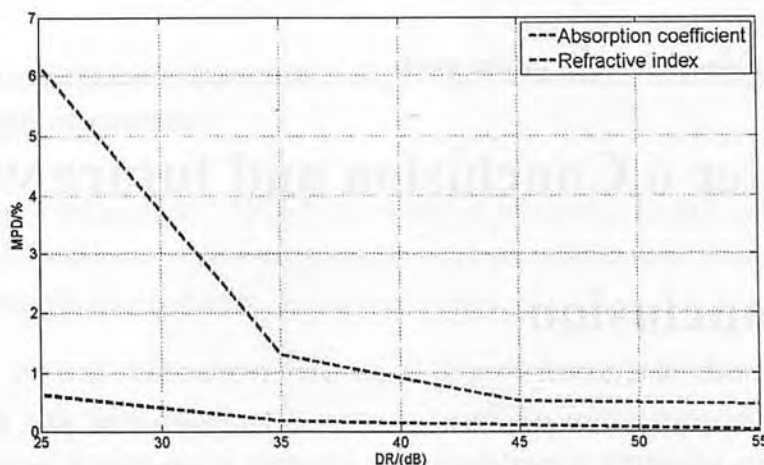
Figure 5.6: Relationship between MPD and DR

5.3.4 Conclusion

In conclusion, after this simulation work, we would choose to DR to evaluate the signal quality of raw data from our scanning system instead of SNR as it is hard to define an accurate noise level for SNR such that before we put the raw data to go through all the calculations mentioned we should make sure the DR of the data is not abnormally low otherwise we should give up that data instead we should select another set of data. And we found that the percentage difference at a particular frequency was quantitatively related to its corresponding DR of the sample signal, such that we have to make sure that the frequency range for the analysis should not be too high.

Chapter 6 Conclusion and future work

6.1 Conclusion

In order to explore the potential of terahertz imaging to be part of the next generation of medical imaging techniques (particularly for the purpose of tissue characterization) and proving the reliability of terahertz, this work started up pilot studies and refined the existing terahertz pulsed imaging techniques. The following are a description of the contribution from this thesis.

6.1.1 A summary of Terahertz pulsed imaging (TPI) techniques

In order to allow the readers of this thesis to have more understanding about terahertz before entering the our measuring work we described the detail of terahertz which include the source, development history and potential applications just at the beginning of the thesis with avoiding to use some too complicated terminology. At the end of chapter 1 we show a clear picture for the structure of this work.

6.1.2 Our system and calculations

For the sake of practical (both in-*vivo* and ex-*vivo*) medical measurement, we chose a TPI system in reflection geometry with a hand-held probe inside this study from TeraView Ltd, Cambridge UK. We showed all the structure and the operation mechanism involved in this system in chapter 2. By doing this we hope the viewer can have a clearer understanding of our work.

Typical reflection systems with an image window usually suffer from ringing artefacts due to the lower surface of the window. In our system using optical parameters of water and air, we were able to determine the baseline and the ringing effects and then account for them in subsequent calculations. Improved accuracy provided further validation of our theories and methods. After determining the baseline effect, with a view to extract the information from the data, we developed a series of operations, which are shown in the second section of chapter 2, for the

analysis of the terahertz signal in both time and frequency domain.

6.1.3 Terahertz spectroscopy of liver cirrhosis: investigating the origin of contrast.

In Chapter 4 we presented TPI *ex vivo* results of rat tissues. In this study we found that refractive indices and absorption coefficients in cirrhotic livers were recognized to be consistently greater than those in normal livers.

And we showed thatterahertz imaging is able to detect both changes in water content and structural changes that occur in tissue due to the presence of cirrhosis whose successful result really give us a great confidence to carry on more other new applications. Our ultimate goal of this experiment is to establish TPI as a reliable tool that can be used for disease diagnosis. Thus, we further employed TPI to study infectious tissues.

6.1.4 In-*vivo* study: skin measurement

To prove that the TPI technique can be part of the next generation of medical imaging diagnosis techniques, *in-vivo* study is necessary. We chose skin to be our *in-vivo* experiment study target. In this study TPI was used to measure the skin on five different locations; namely the forehead, cheek, chin, dorsal forearm, palm at different temperatures. We found that the resulting waveforms from the dorsal forearm and palm measured using the new THz probe were consistent with the previous work using the flatbed imaging system[33]. We found that the cold weather affected the skin properties such that the resulting waveforms were reduced in amplitude. Characterizing different skin areas is important because if TPI is to be used to diagnose skin cancer in the future, the THz properties of healthy skin must be well understood first. This will potentially benefit research into diseases such as skin cancer and other epithelial cancers, and is a first step towards understanding the origin of contrast in THz pulsed images of skin cancer.

6.1.5 SNR sensitivity

In Chapter 5, the system performance was evaluated in terms of SNR and DR. Both of them decreased as the frequency increased, which meant that the signal quality was deteriorating at the higher frequencies. Through simulation work, we found that both the refractive index and absorption coefficient were similarly affected by noise. We further developed a method to quantitatively evaluate the accuracy from the DR values of the sample signal.

6.2 Suggestions for future work

6.2.1 Algorithms

One of our core works is to extract the optical parameters (both absorption coefficient and refractive index) from the measuring sample. However our algorithms for optical parameter extraction were based on the assumption that later reflections after the quartz/sample interface could not be detected. Therefore we can only apply our calculation on homogenous and strongly absorbing objects like fresh tissues with high water content and that is why the study about skin did not involve the calculation of optical parameters. In addition, there would be multiple reflections (See Figure 6.1)reflected off the thin layers sample which could sometimes superimpose on each other and consequently can hardly be separated from each other. Therefore, more theoretical work and simulation needs to be done to study this effect.

Sample

Quartz
plate
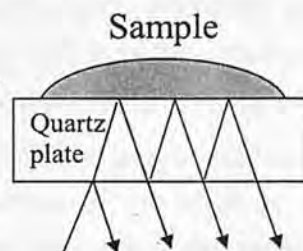
Figure 6.1: A graph showing the multiple reflections.

6.2.2 Understanding the origin of contrast

TPI was further demonstrated to be able to characterize differences between tissues. Although we found some clues to understand them, for example, from their different water content and structural components, these still need to be further validated. Once they can be related with histological examinations, theoretical models may be developed for clinical purposes, for example to predict the water level of a tissue or concentration of a particular chemical composition.

6.2.3 Application in cardiovascular diagnosing imaging

Cardiovascular disease has long been the leading cause of death ·in developed countries, and it is rapidly becoming the number one killer in the world [79, 80]. Atherosclerotic cardiovascular disease is the current leading cause of death in industrialized countries. There is an urgent need to discern different types of plaques (vulnerable, unstable and stable) therefore recognition of the role of the vulnerable plaque has opened new avenues of opportunity in the field of cardiovascular medicine.
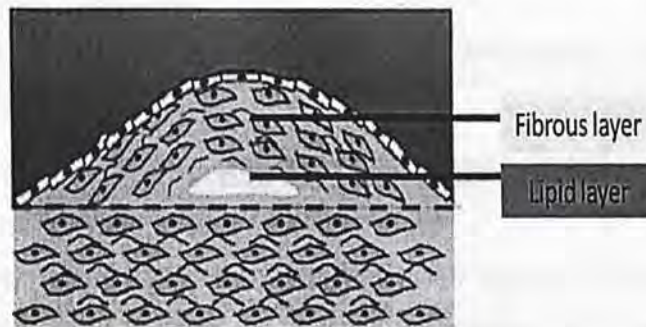
Figure 6.2: A cross-sectional view of a plaque inside an artery.[80]

Generally we can divide the plague in two layers which are fibrous layer and lipid layer shown in Figure 6.2 and the main criterion to classify the type of plague is the thickness of the lipid cap. Normally the thickness of a plaque ranges from 60 μm to 150 μm which terahertz radiation is able to penetrate.

Regarding the characteristic of terahertz radiation being non-ionizing, it is possible to make use of terahertz to be a kind of plague diagnosis technique. During the measurement, we can just model the plaque as a subject with two consistent layers as shown in Figure 6.3. By measuring the distance of the peak in the reflected waveform, we can know the thickness of lipid layer which would help paramedic stuff to diagnosis the plaque.
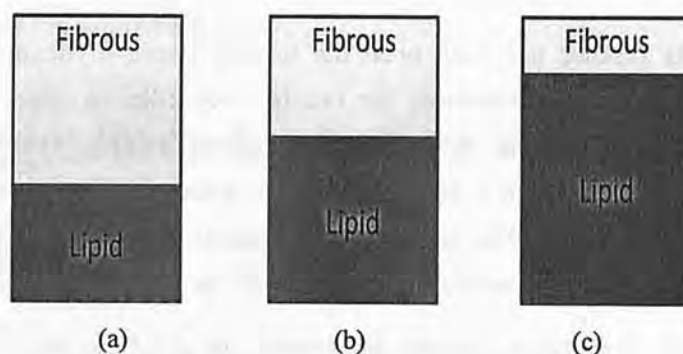
Figure 6.3: A cross-sectional view of different level of plaque inside a artery.

6.3 Concluding remarks

THz imaging is a rapidly developing field but still remains in an early stage, however this thesis has shown that it has great potential to be a valuable imaging technique in the future. A key advantage of THz imaging is that it uses non-ionizing radiation. In the past decade, THz imaging applications in biomedical fields have drawn extensive interest and advances relating to theories, experimental protocols, imaging methods and accuracy of results have been achieved. But there is still a long way to go before it can be clinically used.

References

[1]   S. W. Smye and et al., "The interaction between Terahertz radiation and biological tissue," *Physics in Medicine and Biology,* vol. 46, p. R101, 2001.

[2]   E. F. Nichols, "A method for energy measurements in the infra-red spectrum and the properties of the ordinary ray in quartz for waves of great wave length," *Physical Review (Series I),* vol. 4, p. 297, 1897.

[3]   H. Rubens and E. F. Nichols, "Heat Rays Of Great Wave Length," *Physical Review (Series I),* vol. 4, p. 314, 1897.

[4]   D. Grischkowsky, S. Keiding, M. v. Exter, and C. Fattinger, "Far-infrared time-domain spectroscopy with terahertz beams of dielectrics and semiconductors," *J. Opt. Soc. Am. B,* vol. 7, pp. 2006-2015, 1990.

[5]   C. K. Walker and C. A. Kulesa, "Terahertz astronomy from the coldest place on earth," in *Infrared and Millimeter Waves and 13th International Conference on Terahertz Electronics, 2005. IRMMW-THz 2005. The Joint 30th International Conference on,* 2005, pp. 3-4 vol. 1.

[6]   W. Withayachumnankul, G. M. Png, Y. Xiaoxia, S. Atakaramians, I. Jones, L. Hungyen, U. Seam Yu, *et al.,* "T-Ray Sensing and Imaging," *Proceedings of the IEEE,,* vol. 95, pp. 1528-1558, 2007.

[7]   M. Hoffmann, B. M. Fischer, and P. U. Jepsen, "Terahertz Spectroscopy of RNA and DNA and Spot Array Imaging," 2005.

[8]   Y. Sun and E. Pickwell-MacPherson, "Non-invasive tablet inspection using terahertz pulsed imaging," presented at the Medical Devices and Biosensors, 2008. ISSS-MDBS 2008. 5th *Int.* Summer School and *Symp.*, 2008.

[9]   Y. Sun, M. Y. Sy, Y. X. Wang, A. T. Ahujab, Y. T. Zhang, and E. Pickwell-MacPherson, "A Promising Diagnostic Method – Terahertz Pulsed Imaging and Spectroscopy," *World Journal of Radiology,* 2010.

[10]   D. M. Mittleman, M. Gupta, R. Neelamani, R. G. Baraniuk, J. V. Rudd, and M. Koch, "Recent advances in terahertz imaging," *Applied Physics B: Lasers and Optics,* vol. 68, pp. 1085-1094, 1999.

[11]   X. C. Zhang, "Terahertz wave imaging: horizons and hurdles," *Physics in Medicine and Biology,* vol. 47, p. 3667, 2002.

[12]   P. H. Siegel, "Terahertz technology in biology and medicine," *IEEE, Transactions on Microwave Theory and Techniques,* vol. 52, pp. 2438-2447, 2004.

[13]   V. P. Wallace, P. F. Taday, A. J. Fitzgerald, R. M. Woodward, J. Cluff, R. J. Pye, and D. D. Arnone, "Terahertz pulsed imaging and spectroscopy for biomedical and pharmaceutical applications," *Faraday Discussions,* vol. 126, pp. 255-263, 2004.

[14]   E. R. Brown, K. A. Mcintosh, K. B. Nichols, and C. L. Dennis, "Photomixing up to 3.8-Thz in Low-Temperature-Grown Gaas," *Applied Physics Letters,* vol. 66, pp. 285-287, Jan 16 1995.

7. References

[15]   Y. U. Jeong, B. C. Lee, S. K. Kim, S. O. Cho, B. H. Cha, J. Lee, G. M. Kazakevitch, *et al.*, "First lasing of the KAERI compact far-infrared free-electron laser driven by a magnetron-based microtron," *Nuclear Instruments & Methods in Physics Research Section a-Accelerators Spectrometers Detectors and Associated Equipment,* vol. 475, pp. 47-50, Dec 21 2001.

[16]   J. H. Smet, C. G. Fonstad, and Q. Hu, "Intrawell and interwell intersubband transitions in multiple quantum wells for far-infrared sources," *Journal of Applied Physics,* vol. 79, pp. 9305-9320, Jun 15 1996.

[17]   D. H. Auston, "Picosecond optoelectronic switching and gating in silicon," *Applied Physics Letters,* vol. 26, pp. 101-103, 1975.

[18]   X. C. Zhang, X. F. Ma, Y. Jin, T. M. Lu, E. P. Boden, P. D. Phelps, K. R. Stewart, *et al.*, "Terahertz Optical Rectification from a Nonlinear Organic-Crystal," *Applied Physics Letters,* vol. 61, pp. 3080-3082, Dec 28 1992.

[19]   R. Huber, F. Tauser, A. Brodschelm, M. Bichler, G. Abstreiter, and A. Leitenstorfer, "How many-particle interactions develop after ultrafast excitation of an electron-hole plasma," *Nature,* vol. 414, pp. 286-289, 2001.

[20]   H. G. Roskos, M. C. Nuss, J. Shah, K. Leo, D. A. B. Miller, A. M. Fox, S. Schmittrink, *et al.*, "Coherent Submillimeter-Wave Emission from Charge Oscillations in a Double-Well Potential," *Physical Review Letters,* vol. 68, pp. 2216-2219, Apr 6 1992.

[21]   K. McClatchey, M. T. Reiten, and R. A. Cheville, "Time resolved synthetic aperture terahertz impulse imaging," *Applied Physics Letters,* vol. 79, pp. 4485-4487, 2001.

[22]   N. Karpowicz, H. Zhong, J. Z. Xu, K. I. Lin, J. S. Hwang, and X. C. Zhang, "Comparison between pulsed terahertz time-domain imaging and continuous wave terahertz imaging," *Semiconductor Science and Technology,* vol. 20, pp. S293-S299, Jul 2005.

[23]   S. W. Smye, J. M. Chamberlain, A. J. Fitzgerald, and E. Berry, "The interaction between Terahertz radiation and biological tissue," *Physics in Medicine and Biology,* vol. 46, pp. R101-R112, Sep 2001.

[24]   W. C. KAN, "Terahertz Pulsed Imaging of Osteoarthritis Joint Cartilage," Master of Philosophy, Electronic Engineering, The Chinese University of Hong Kong 2009.

[25]   D. D. Arnone, C. M. Ciesla, A. Corchia, S. Egusa, M. Pepper, J. M. Chamberlain, C. Bezant, *et al.*, "Applications of Terahertz (THz) technology to medical imaging," *Terahertz Spectroscopy and Applications II,* vol. 3828, pp. 209-219, 1999.

[26]   P. Y. Han, G. C. Cho, and X. C. Zhang, "Time-domain transillumination of biological tissues with terahertz pulses," *Optics Letters,* vol. 25, pp. 242-244, Feb 15 2000.

[27]   T. Loffler, K. Siebert, S. Czasch, T. Bauer, and H. G. Roskos, "Visualization and classification in biomedical terahertz pulsed imaging," *Physics in Medicine and Biology,* vol. 47, pp. 3847-3852, Nov 7 2002.

[28]   P. Knobloch, C. Schildknecht, T. Kleine-Ostmann, M. Koch, S. Hoffmann, M. Hofmann, E. Rehberg, *et al.*, "Medical THz imaging: an investigation of histo-pathological samples," *Physics in Medicine and Biology,* vol. 47, pp. 3875-3884, Nov 7 2002.

[29]   B. Ferguson, S. Wang, D. Gray, D. Abbott, and X. C. Zhang, "Identification of biological tissue using chirped probe THz imaging," *Microelectronics Journal,* vol. 33, pp. 1043-1051, 2002.

7. References

[30]   R. M. Woodward, V. P. Wallace, D. D. Arnone, E. H. Linfield, and M. Pepper, "Terahertz Pulsed Imaging of Skin Cancer in the Time and Frequency Domain," *Journal of Biological Physics,* vol. 29, pp. 257-259, 2003.

[31]   E. Berry, A. J. Fitzgerald, N. N. Zinov'ev, G. C. Walker, S. Homer-Vanniasinkam, C. D. Sudworth, R. E. Miles, *et al.*, "Optical properties of tissue measured using terahertz pulsed imaging," *Medical Imaging 2003: Physics of Medical Imaging, Pts 1 and 2,* vol. 5030, pp. 459-470, 2003.

[32]   A. J. Fitzgerald, E. Berry, N. N. Zinov'ev, S. Homer-Vanniasinkam, R. E. Miles, J. M. Chamberlain, and M. A. Smith, "Catalogue of Human Tissue Optical Properties at Terahertz Frequencies," *Journal of Biological Physics,* vol. 29, pp. 123-128, 2003.

[33]   E. Pickwell, B. E. Cole, A. J. Fitzgerald, M. Pepper, and V. P. Wallace, "In vivo study of human skin using pulsed terahertz radiation," *Phys. Med. Biol.,* vol. 49, p. 1595, 2004.

[34]   V. P. Wallace, A. J. Fitzgerald, E. Pickwell, R. J. Pye, P. F. Taday, N. Flanagan, and T. Ha, "Terahertz pulsed spectroscopy of human basal cell carcinoma," *Applied Spectroscopy,* vol. 60, pp. 1127-1133, Oct 2006.

[35]   M. X. He, A. K. Azad, S. H. Ye, and W. L. Zhang, "Far-infrared signature of animal tissues characterized by terahertz time-domain spectroscopy," *Optics Communications,* vol. 259, pp. 389-392, Mar 1 2006.

[36]   S. Nakajima, H. Hoshina, M. Yamashita, C. Otani, and N. Miyoshi, "Terahertz imaging diagnostics of cancer tissues with a chemometrics technique," *Applied Physics Letters,* vol. 90, pp. -, Jan 22 2007.

[37]   E. Pickwell-MacPherson, T. Lo, A. Fitzgerald, E. Provenzano, S. Pinder, A. Purushotham, and V. P. Wallace, "Application of Finite Difference Time Domain methods to Terahertz Spectroscopy Measurements of Breast Cancer," in *Microwave Symposium, 2007. IEEE/MTT-S International,* 2007, pp. 1379-1381.

[38]   G. M. Png, J. W. Choi, B. W.-H. Ng, S. P. Mickan, D. Abbott, and X.-C. Zhang, "The impact of hydration changes in fresh bio-tissue on THz spectroscopic measurements," *Physics in Medicine and Biology,* vol. 53, pp. 3501-3517, 2008.

[39]   H. Hoshina, A. Hayashi, N. Miyoshi, F. Miyamaru, and C. Otani, "Terahertz pulsed imaging of frozen biological tissues," *Applied Physics Letters,* vol. 94, pp. -, Mar 23 2009.

[40]   B. M. Fischer, M. Hoffmann, H. Helm, R. Wilk, F. Rutz, T. Kleine-Ostmann, M. Koch, *et al.*, "Terahertz time-domain spectroscopy and imaging of artificial RNA," *Optics Express,* vol. 13, pp. 5205-5215, Jul 11 2005.

[41]   R. M. Woodward and et al., "Terahertz pulse imaging in reflection geometry of human skin cancer and skin tissue," *Physics in Medicine and Biology,* vol. 47, p. 3853, 2002.

[42]   R. M. Woodward, V. P. Wallace, B. E. Cole, R. J. Pye, D. D. Arnone, E. H. Linfield, and M. Pepper, "Terahertz pulse imaging in reflection geometry of skin tissue using time-domain analysis techniques," San Jose, CA, USA, 2002, pp. 160-169.

[43]   A. J. Fitzgerald, V. P. Wallace, M. Jimenez-Linan, L. Bobrow, R. J. Pye, A. D. Purushotham, and D. D. Arnone, "Terahertz Pulsed Imaging of Human Breast Tumors1," *Radiology,* vol. 239, pp. 533-540, May 2006 2006.

[44]   E. Pickwell, V. P. Wallace, B. E. Cole, S. Ali, C. Longbottom, R. J. Lynch, and M. Pepper, "Using Terahertz Pulsed Imaging to Measure Enamel Demineralisation in Teeth," presented at

7. References

the Infrared Millimeter Waves and 14th *Int. Conf.* on Teraherz Electronics, 2006. IRMMW-THz 2006. Joint 31st *Int. Conf.*, 2006.

[45] S. Y. Huang, Y. X. Wang, D. K. W. Yeung, V. P. Wallace, Y. T. Zhang, and E. Pickwell-MacPherson, "Characterizing rat tissue samples using Terahertz Pulsed Imaging," presented at the Infrared, Millimeter and Terahertz Waves, 2008. IRMMW-THz 2008. 33rd *Int. Conf.*, 2008.

[46] S. Y. Huang, P. C. Ashworth, K. W. Kan, Y. Chen, V. P. Wallace, Y.-t. Zhang, and E. Pickwell-MacPherson, "Improved sample characterization in terahertz reflection imaging and spectroscopy," *Opt. Express,* vol. 17, pp. 3848-3854, 2009.

[47] M. Sherwin, "Applied physics: Terahertz power," *Nature,* vol. 420, pp. 131-133, 2002.

[48] R. Kohler, A. Tredicucci, F. Beltram, H. E. Beere, E. H. Linfield, A. G. Davies, D. A. Ritchie, *et al.*, "Terahertz semiconductor-heterostructure laser," *Nature,* vol. 417, pp. 156-159, 2002.

[49] B. Fischer, M. Hoffmann, H. Helm, R. Wilk, F. Rutz, T. Kleine-Ostmann, M. Koch, *et al.*, "Terahertz time-domain spectroscopy and imaging of artificial RNA," *Opt. Express,* vol. 13, pp. 5205-5215, 2005.

[50] F. X. Bosch, J. Ribes, M. Diaz, and R. Cleries, "Primary liver cancer: Worldwide incidence and trends," *Gastroenterology,* vol. 127, pp. S5-S16, Nov 2004.

[51] U. C. Nzeako, Z. D. Goodman, and K. G. Ishak, "Hepatocellular carcinoma in cirrhotic and noncirrhotic livers - A clinico-histapathologic study of 804 North American patients," *American Journal of Clinical Pathology,* vol. 105, pp. 65-75, Jan 1996.

[52] J. M. Llovet, J. Fuster, J. Bruix, and B. C. L. C. Grp, "Intention-to-treat analysis of surgical treatment for early hepatocellular carcinoma: Resection versus transplantation," *Hepatology,* vol. 30, pp. 1434-1440, Dec 1999.

[53] M. Lanthaler, M. Biebl, A. Weissenbacher, R. Margreiter, and H. Nehoda, "Recurrence after liver resection for hepatocellular carcinoma in cirrhotic and noncirrhotic patients," *Chirurgische Gastroenterologie,* vol. 24, pp. 51-54, 2008.

[54] A. P. O'Rourke, M. Lazebnik, J. M. Bertram, M. C. Converse, S. C. Hagness, J. G. Webster, and D. M. Mahvi, "Dielectric properties of human normal, malignant and cirrhotic liver tissue: in vivo and ex vivo measurements from 0.5 to 20 GHz using a precision open-ended coaxial probe," *Phys. Med. Biol.,* vol. 52, pp. 4707-4719, 2007.

[55] C. H. Janes and K. D. Lindor, "Outcome of Patients Hospitalized for Complications after Outpatient Liver Biopsy," *Annals of Internal Medicine,* vol. 118, pp. 96-98, 1993.

[56] J. Poniachik, D. E. Bernstein, K. R. Reddy, L. J. Jeffers, M. E. Coelho-Little, F. Civantos, and E. R. Schiff, "The role of laparoscopy in the diagnosis of cirrhosis," *Gastrointest Endosc,* vol. 43, pp. 568-71, Jun 1996.

[57] A. A. Bravo, S. G. Sheth, and S. Chopra, "Liver biopsy," *N Engl J Med,* vol. 344, pp. 495-500, 2001.

[58] Y. Watanabe, K. Kawase, T. Ikari, H. Ito, Y. Ishikawa, and H. Minamide, "Component spatial pattern analysis of chemicals using terahertz spectroscopic imaging," *Applied Physics Letters,* vol. 83, pp. 800-802, 2003.

[59] D. Bigourd, A. Cuisset, F. Hindle, S. Matton, R. Bocquet, G. Mouret, F. Cazier, *et al.*, "Multiple component analysis of cigarette smoke using THz spectroscopy, comparison with

standard chemical analytical methods," *Applied Physics B: Lasers and Optics,* vol. 86, pp. 579-586, 2007.

[60]   P. U. Jepsen, U. Møler, and H. Merbold, "Investigation of aqueous alcohol and sugar solutions with reflection terahertz time-domain spectroscopy," *Opt. Express,* vol. 15, pp. 14717-14737, 2007.

[61]   Y. Sun, B. M. Fischer, and E. Pickwell-MacPherson, "The effects of formalin fixing on terahertz image contrast," *J. Biomedical Optics,* vol. 14, p. 064017, Dec 2009.

[62]   M. H. Hofker and J. V. Deursen, *Methods in Molecular Biology.* New Jersey: Humana Press, 2002.

[63]   L. C. Junqueira, *Basic histology : text & atlas.* New York: McGraw-Hill, 2005.

[64]   S. Y. Huang, Y. J. Wang, D. K. W. Yeung, A. T. Ahuja, Y. T. Zhang, and E. Pickwell-MacPherson, "Tissue characterization using terahertz pulsed imaging in reflection geometry," *Phys. Med. Biol.,* vol. 54, pp. 149-160, 2009.

[65]   A. P. O'Rourke, M. Lazebnik, J. M. Bertram, M. C. Converse, S. C. Hagness, J. G. Webster, and D. M. Mahvi, "Dielectric properties of human normal, malignant and cirrhotic liver tissue: in vivo and ex vivo measurements from 0.5 to 20 GHz using a precision open-ended coaxial probe," *Phys. Med. Biol.,* vol. 52, p. 4707, 2007.

[66]   E. Pickwell, "Biological Applications of Terahertz Pulsed Imaging and Spectroscopy," Doctor of Philosophy, Cambridge University, 2005.

[67]   A. J. Fitzgerald, V. P. Wallace, R. Pye, M. Jimenez-Linan, L. Bobrow, A. D. Purushotham, and D. D. Arnone, "Terahertz imaging of breast cancer, a feasibility study," presented at the Infrared and Millimeter Waves, 2004 and 12th *Int. Conf.* on Terahertz Electronics, 2004. Conference Digest of the 2004 Joint 29th *Int. Conf.,* 2004.

[68]   P. T. Pugliese, *Physiology of the skin II : an expanded scientific guide for the skin care professiona*: Carol Stream, IL:Allured Pub. Corp, 2001.

[69]   M. Y. Sy, Y. Chen, Y. T. Zhang, and E. Pickwell-Macphersone, "A Study of Terahertz Pulsed Imaging of Human Skin," presented at the The 6th International School and Symposium on Medical Devices and Biosensors, in conjunction with The 4th International School and Symposium on Biomedical and Health Engineering,, Shenzhen,, December 2009.

[70]   Gao Tianwen and L. Wenjun, *Pi fu zu zhi bing li xue ru men : pi fu ke yi shi de bi bei zhi shi = The entrance to dermatopathology,*: Beijing Shi : Ren min wei sheng chu ban she, 2007,.

[71]   P. Hermann, *A guide to dermatohistopathology / [by] Hermann Pinkus [and] Amir H. Mehregan,* . New York Appleton-Century-Crofts, 1969.

[72]   A. Poppe, L. Xu, F. Krausz, and C. Spielmann, "Noise characterization of Sub-10-fs Ti : sapphire oscillators," in *Meeting on Ultrafast Optics,* Monterey, California, 1998, pp. 179-184.

[73]   L. Duvillaret, F. Garet, J. F. Roux, and J. L. Coutaz, "Analytical modeling and optimization of terahertz time-domain spectroscopy experiments using photoswitches as antennas," *Ieee Journal of Selected Topics in Quantum Electronics,* vol. 7, pp. 615-623, Jul-Aug 2001.

[74]   D. M. Mittleman, R. H. Jacobsen, and M. C. Nuss, "T-ray imaging," *Selected Topics in Quantum Electronics, IEEE Journal of,* vol. 2, pp. 679-692, 1996.

[75]   G. Zhao, R. N. Schouten, N. van der Valk, W. T. Wenckebach, and P. C. M. Planken, "Design

7. References

and performance of a THz emission and detection setup based on a semi-insulating GaAs emitter," *Review of Scientific Instruments*, vol. 73, pp. 1715-1719, Apr 2002.

[76]   S. Jay and R. C. Alan, "Noise reduction in THz systems using THz interferometry," in *Conference on Lasers and Electro-Optics/International Quantum Electronics Conference and Photonic Applications Systems Technologies*, 2004, p. CTuB5.

[77]   B. Ferguson and D. Abbott, "De-noising techniques for terahertz responses of biological samples," *Microelectronics Journal*, vol. 32, pp. 943-953, 2001.

[78]   M. Naftaly and R. Dudley, "Methodologies for determining the dynamic ranges and signal-to-noise ratios of terahertz time-domain spectrometers," *Optics Letters*, vol. 34, pp. 1213-1215, Apr 15 2009.

[79]   M. Naghavi, P. Libby, E. Falk, S. W. Casscells, S. Litovsky, J. Rumberger, J. J. Badimon, *et al.*, "From Vulnerable Plaque to Vulnerable Patient: A Call for New Definitions and Risk Assessment Strategies: Part I," *Circulation*, vol. 108, pp. 1664-1672, October 7, 2003 2003.

[80]   J. G. Kips, P. Segers, and L. M. Van Bortel, "Identifying the vulnerable plaque: A review of invasive and non-invasive imaging modalities," *Artery Research*, vol. 2, pp. 21-34, 2008.